



Deciphering interseismic strain accumulation and its termination on the central-eastern Altyn Tagh fault from high-resolution velocity fields

Dehua Wang, John R. Elliott, Gang Zheng^{*}, Tim J. Wright, Andrew R. Watson, Jack D. McGrath

COMET, School of Earth and Environment, University of Leeds, Leeds, UK

ARTICLE INFO

Editor: J.P. Avouac

Keywords:

Altyn Tagh fault
Qilian Shan – Nan Shan thrust belt
Strain accumulation
Slip Partitioning
Sentinel-1 InSAR
Restraining Bends

ABSTRACT

Investigating the present-day pattern of strain accumulation along the Altyn Tagh fault (ATF) in northwestern Tibet is critical for our broader understanding of deformation around large active strike-slip faults and the associated seismic hazards. Previous geodetic and geological studies show an eastward decrease of slip rate along the central-eastern ATF, but the spatial variation of the slip rates and the mechanism causing such variation are uncertain. Additionally, interseismic deformation around the restraining bends along the ATF and its pattern of termination towards its eastern end are also unclear. Here we derive surface velocities and strain rates around the central-eastern ATF system using Sentinel-1 and GNSS velocities. We estimate fault parameters including slip rate and locking depth for the ATF and other related active faults indicated by our strain rate maps using a Bayesian inversion approach. Our results show shear strain is mainly concentrated on the ATF between 86°E and 95°E. The strike-slip rate of the ATF remains constant at ~8 mm/yr between 86°E and 90.5°E, before decreasing gradually to ~4.5 mm/yr between 90.5°E and 94°E due to the crustal shortening across the Qaidam basin. Shear strain on the ATF is terminated in a horsetail structure at 95°E, where the strain is split into the motion along the Danghe Nanshan fault, Yema River – Daxue Shan fault and north Altyn Tagh fault. Our strain rate fields show fault planes are nearly vertical beneath the ATF, and there are obvious changes in the strike of the deep shearing part of the fault beneath the Akato Tagh bend and Aksay bend. The Akato Tagh and Pingding Shan bends feature higher peak strain rates and narrower width of the interseismic straining zone at the surface, compared to straight sections like the Xorkoli segment. We observe long-wavelength uplift signals in the East Kunlun Shan range, Altun Shan range, Qaidam basin, restraining bends along the ATF and the Qilian Shan – Nan Shan thrust belt. We consider uplift of the latter is controlled by the thrust motion of the active faults within it, as almost all shortening within it occurs across the fault zones. Uplift around restraining bends along the ATF exhibits a larger rate at their inside corners, which is evidence of potential vertical-axis rotation within the bends. Our results provide a noteworthy example of how the strain is accumulated and terminated on a large-scale intra-plate strike-slip fault.

1. Introduction

The Altyn Tagh fault (ATF) is one of the largest strike-slip faults in the world and acts as a major boundary between the Tibetan Plateau and the Tarim Basin (Fig. 1a). Compared to other large-scale strike-slip faults such as the San Andreas fault and the North Anatolian fault, where many large-scale geodetic studies (e.g. Kaneko et al., 2013; X. Xu et al., 2021) have already contributed to a comprehensive understanding of the faults, previous geodetic studies about the ATF are mostly regional, tightly constrained to subsegments of the fault using one to a few

Synthetic Aperture Radar (SAR) swaths only. In the following we introduce several important questions about the active tectonics of the ATF that have not been well answered by previous studies.

Firstly, how does the slip rate vary spatially along the ATF. Fault slip rates are the key parameters when evaluating seismic potential and assessing seismic risk of an area (e.g. Youngs and Coppersmith, 1985). Both geological and geodetic results (e.g. Zhang et al., 2007; Li et al., 2018) reveal that the slip rates on the ATF are not constant along strike but show a significant eastward decrease. Due to the discontinuous distribution of field surveys, low spatial resolution of Global Navigation

^{*} Corresponding author at: Permanent Address: School of Earth and Environment, University of Leeds, Leeds, UK.
E-mail address: G.Zheng@leeds.ac.uk (G. Zheng).

<https://doi.org/10.1016/j.epsl.2024.118919>

Received 31 January 2024; Received in revised form 4 June 2024; Accepted 25 July 2024

Available online 14 August 2024

0012-821X/© 2024 The Authors. Published by Elsevier B.V. This is an open access article under the CC BY license (<http://creativecommons.org/licenses/by/4.0/>).

Satellite System (GNSS) velocities and relatively small scale of previously published Interferometric Synthetic Aperture Radar (InSAR) results, we still lack a clear picture of the spatial variation of current slip rates along the ATF.

The second question to address is how the transpressive strain is accommodated within the ATF system. Oblique-slip faults, strain partitioning (e.g. Panda et al., 2018) and distributed deformation within the blocks (e.g. England and McKenzie, 1982) are three possibilities to accommodate deformation in transpressive zones, each of them causing a distinct surface velocity and strain rate pattern. Due to the sparse GNSS data distribution along the ATF system, the strain pattern within it is still poorly resolved. With new data from the Sentinel-1 radar satellite, we can derive a high-resolution strain rate model (e.g. Wang et al., 2019) and distinguish localized deformation related to active faults and distributed deformation within blocks. Based on such a strain rate

model, we can better understand the balance of on-fault and off-fault deformation in zones of active mountain building around the ATF and the potential seismic hazard for surrounding areas.

The third question relates to how the crust around fault bends along the ATF deforms during the current interseismic period. Restraining or releasing bends are widely distributed along strike-slip faults (Mann, 2007), and they have been identified as loci of both initiation and termination for seismic ruptures (King and Nábělek, 1985), suggesting they play important roles in controlling the size and extent of earthquakes and consequently the seismic hazard around strike-slip fault zones. Four restraining bends and a relatively straight segment, called the Xorkoli segment, can be found along the ATF (Fig. 1a & S1a). For some restraining bends, previous studies have revealed their geometry, topographic features, evolution mechanism, and role in historic earthquakes (Cowgill et al., 2004; Elliott et al., 2015; Shao et al., 2018) and

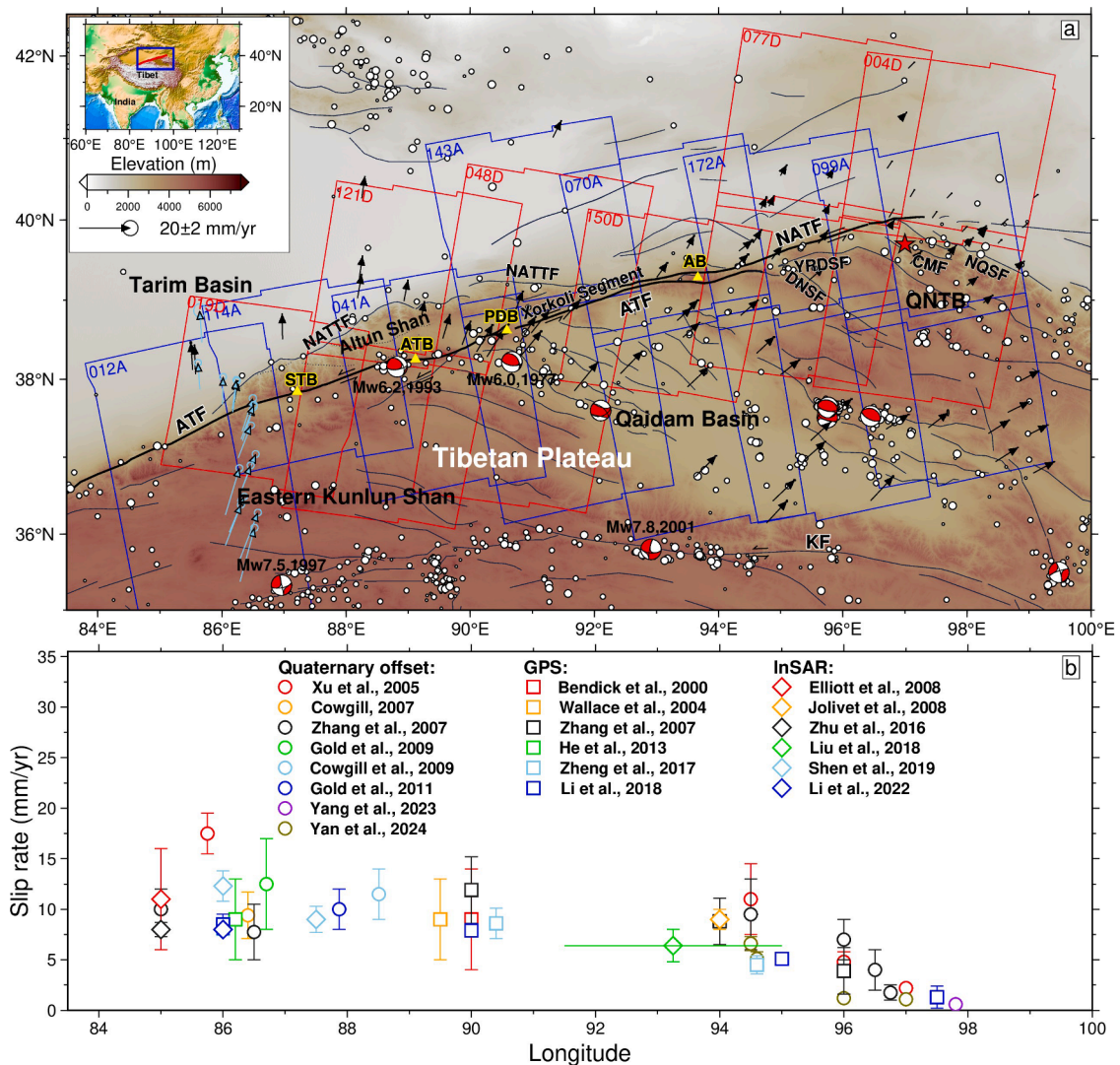


Fig. 1. (a) Tectonic map of the central-eastern Altyn Tagh fault (ATF) and its surrounding areas. Thick black lines represent the high-resolution fault traces of the ATF and north Altyn Tagh fault (NATF) based on studies from Elliott et al. (2015), and thin black lines represent modified surface traces of other important active faults based on Styron & Pagani (2020) and Q. Xu et al. (2021). Yellow triangles mark the centers of active restraining bends along the ATF. Blue and red polygons represent the Sentinel-1 coverage of ascending and descending data, respectively. Black arrows are the GNSS horizontal velocities estimated in this study, and skyblue arrows show modified GNSS velocities based on results from Li et al. (2018). GNSS vertical velocities estimated in this study are shown in Fig. S1. White circles denote earthquakes with moment magnitudes $M_w < 6.0$ from January 1976 to June 2022 based on data from the U.S. Geological Survey. Red focal mechanisms highlight strong earthquakes with magnitudes larger than $M_w 6.0$ based on the data from Global Centroid Moment Tensor Catalog (Dziewonski et al., 1981; Ekström et al., 2012). Red star represents the 1932 Ms 7.6 Changma Earthquake (Du et al., 2020). ATF: Altyn Tagh fault; NATF: north Altyn Tagh fault; NATTF: north Altyn Tagh thrust fault; KF: Kunlun fault; DNSF: Danghe Nanshan fault; YRDSF: Yema River – Daxue Shan fault; CMF: Changma fault; NQSF: north Qilian Shan fault; EKS: East Kunlun Shan range; QNTB: Qilian Shan – Nan Shan thrust belt; STB: Sulamu Tagh bend; ATB: Akato Tagh bend; PDB: Pingding Shan bend; AB: Aksay bend. (b) Previous published slip rates along the central-eastern ATF. The green horizontal line shows the lateral extent of measurement in Liu et al. (2018).

suggested concentrated shortening within the inside corners (Figure S1b) of the bends (Cowgill et al., 2004). However, the current interseismic deformation around the bends has not been well studied using geodetic data.

The fourth question concerns how the ATF terminates at its eastern end. A previous study (Withers et al., 2023) showed that the termination pattern of a transform fault depends on how such a fault is connected with other plate boundaries. A “seamless” and continuous transition zone will form if they are well-connected (e.g. the northern termination of the Alpine fault), while a distributed transition zone will be observed if they are “misaligned” (e.g. the southern termination of the San Andreas fault). How intra-plate strike-slip faults (e.g. ATF) terminate has not been systematically studied. Some hypotheses (e.g., Xu et al., 2005) have been proposed to interpret the termination pattern of the eastern ATF, but evidence from high-resolution geodetic data is still incomplete.

To address the above questions, we model the surface velocities and strain rates for 1200 km of the central-eastern segments of the ATF using Sentinel-1 InSAR rate maps and GNSS velocities. We also use our velocity field to constrain the best fit values for strike-slip rate, locking depth and fault location for the ATF and other important active faults (indicated by our strain rate maps) following a Bayesian inversion approach. We not only quantify the strain accumulation along the 1200-km-long central-eastern ATF but also explore their implications for understanding the deformation around fault bends, mountain building and pattern of fault termination.

2. Review of geological and geodetic slip rate estimates for the ATF

Previous slip rates have been measured at different locations along the central-eastern ATF using both geological methods (e.g. terrace offsets and dating ages) and geodetic methods (e.g. GNSS and InSAR). For the segment between 85°E and 91°E, some early geological results estimated large slip rates of over 20 mm/yr (e.g. Mériaux et al., 2004), but more recent geological results show slip rates of 6–15 mm/yr (e.g. Cowgill, 2007; Cowgill et al., 2009; Gold et al., 2009; Gold et al., 2011) (Fig. 1b), which is consistent with the results from InSAR (e.g. Elliott et al., 2008; Zhu et al., 2016; Shen et al., 2019; Li et al., 2022) and GNSS data (e.g. Bendick et al., 2000; Wallace et al., 2004; He et al., 2013; Zheng et al., 2017; Li et al., 2018) (Fig. 1b).

How the slip rates change further east along the segment between 91°E and 95°E is less clear, and there are no geological estimates between 89°E and 94°E. Some geological results showed slip rates of ~10 mm/yr at ~94.5°E (11 ± 3.5 mm/yr, Xu et al., 2005; 9.5 ± 3.5 mm/yr, Zhang et al., 2007) (Fig. 1b), which is supported by slip rates of ~9 mm/yr derived from InSAR (9 ± 1 mm/yr, Jolivet et al., 2008) and GNSS data (8.8 ± 2.3 mm/yr, Zhang et al., 2007) at ~94°E (Fig. 1b), suggesting that there might be no significant change of slip rates around ~94°E. Liu et al. (2020) suggested the slip rates decrease sharply from ~10 mm/yr to ~5 mm/yr between 94°E and 95°E by estimating the late Quaternary slip rates on four sites near the Aksay Bend based on river terraces, which supports the large fault slip rates observed near 94°E (8.8 ± 2.3 mm/yr, Zhang et al., 2007; 9 ± 1 mm/yr, Jolivet et al., 2008) and the small fault slip rates around 95°E (4.5 ± 0.9 mm/yr, Zheng et al., 2017; 5.1 ± 0.6 mm/yr, Li et al., 2018) (Fig. 1b). However, results of slip rates of 6.4 ± 1.6 mm/yr for the segment between 91.5°E and 95°E from InSAR (Liu et al., 2018) (Fig. 1b) and profiles of fault-parallel velocities at two sides of the ATF from GNSS data (Zhang et al., 2007) indicate that the slip rates may begin to decrease further west than 94°E.

Small slip rates of ~4 mm/yr on the north Altyn Tagh fault (NATF) between 95°E and 96°E have been reported by both geological (4.8 ± 1 mm/yr, Xu et al., 2005) and geodetic measurements (3.9 ± 2.3 mm/yr, Zhang et al., 2007; 5.1 ± 0.6 mm/yr, Li et al., 2018) (Fig. 1b), and the slip rates continue to decrease to ~1 mm/yr at ~98°E (1.3 ± 1.1 mm/yr, Li et al., 2018; 0.6 ± 0.2 mm/yr, Yang et al., 2023) (Fig. 1b). The cause for the decrease of slip rates on the NATF has not been well quantified in

previous results, nor how slip is accommodated on other faults. A recent geological study (Yan et al., 2024) shows the slip rate on the NATF at 96°E is 1.2 ± 0.1 mm/yr (Fig. 1b), which is much lower than earlier geological results (4.8 ± 1 mm/yr, Xu et al., 2005; 7 ± 2 mm/yr, Zhang et al., 2007), suggesting there may be a big uncertainty in geological slip rates.

3. Data and methods

3.1. GNSS data and processing

We collected raw GNSS data covering 1998–2021 from both the CMONOC-I and CMONOC-II projects. We used GAMIT/GLOBK software (Herring et al., 2018), version 10.7, to process our own GNSS network solution with the strategy of Wang et al. (2022) and obtain the positioning time-series in the ITRF2014 reference frame (Altamimi et al., 2016). Effects from major earthquakes during the timespan of our GNSS data were removed following the strategy of Zheng et al. (2017), which involves removing the coseismic offsets and the affected postseismic data so as not to be modeling the postseismic deformation. We used the Hector software (Bos et al., 2013) to model the positioning time series to obtain 3D velocities at each GNSS station. We apply trigonometric functions to fit the annual and semi-annual signals, which can improve the reliability of the velocities, especially for the vertical component. The horizontal velocities were then transformed into the Eurasia-fixed reference frame according to the ITRF2014-Eurasia Euler vector (Altamimi et al., 2017). Thus, we obtained our core GNSS velocity field with 78 CMONOC-I/II stations, including 8 continuous and 70 campaign stations. Li et al. (2018) compiled a regional GNSS velocity field for the ATF, and it includes a GNSS profile with 17 stations which are not included in our CMONOC-I/II solution. We calculated a Euler vector which best fits the velocity differences at the common stations between our velocity field and Li et al. (2018)'s, and then applied this to convert Li et al. (2018)'s velocities at the 17 stations into our CMONOC-I/II solution by rigid body rotation. Such conversion only results in changes of less than 1 mm/yr relative to the velocities in Li et al. (2018). Our resultant GNSS velocity field comprises 95 stations in total (Fig. 1a).

3.2. Sentinel-1 InSAR data and processing

We use the LiCSAR system (Lazecqy et al., 2020) to derive interferogram networks, which are multi-looked by 20 in range and 4 in azimuth (~50 m), and then downsampled to 100 m resolution. We processed 11 LiCSAR frames on 7 ascending tracks and 9 LiCSAR frames on 6 descending tracks (Fig. S2). For each frame, we used ~170 acquisition epochs (Table S1 & S2) between October 2014 and July 2022. LiCSAR normally generates interferograms between each epoch and four consecutive epochs both forwards and backwards in time by default, but here we combined short baselines with 1-year to 7-year long temporal summer-to-summer baselines in the network (Fig. S3 & S4), which not only reduces potential phase biases related to relatively short temporal baselines (e.g. Ansari et al., 2021), but also reduces the impact of snow cover on capturing the deformation signals of the mountains in winter. In total we used ~2000 interferograms in each frame (Table S1 & S2) after bad interferograms (e.g. those with swath discontinuities, coregistration errors and missing bursts) were removed manually.

We carried out time-series analysis using LiCSBAS (Morishita et al., 2020), during which we first downsampled the resolution of all interferograms to 1 km to reduce the computing demands, and then removed estimates of the tropospheric phases for each epoch based on the Generic Atmospheric Correction Online Service (GACOS) (Yu et al., 2018). As the remaining interferograms may still have unwrapping errors, we chose to reduce the impact of such errors by nullifying (removing the values) all the displacements of interferograms associated with an unclosed loop in the time series for each pixel (Figure S5). After obtaining displacement time series of each pixel in a frame, the average

linear velocities were calculated based on the standard approach in LiCSBAS, which is similar to the NSBAS least-squares method (Doin et al., 2011). During the velocity inversion, we do not consider the impact of coseismic deformation from earthquakes that occur near the ATF system during the acquisition period of InSAR data, as the earthquakes are small with magnitudes not larger than M_w 5.1 (Fig. 1a). Additionally, we ignore postseismic deformation due to the absence of significant historic strike-slip earthquakes over the last ~ 300 years (Yuan et al., 2020).

Final line-of-sight (LOS) velocity uncertainties are calculated from the standard deviation (STD) of 100 velocities based on resampled datasets of displacement time series using the bootstrap method, and yield estimates <1 mm/yr (Figure S6). We masked relatively unreliable pixels using several noise evaluation indices such as the average coherence and number of network gaps for each pixel (Morishita et al., 2020) (Fig. S7). The seasonal signals in the time series (Figure S8) may influence our estimation of velocities and their uncertainties. However, as we used ~ 7 -year-long networks to acquire the long-term velocities for each pixel, the impacts from seasonal signals are normally minor. The root mean square of residuals (resid_rms) in the linear velocity inversion are predominately less than 1 mm/yr (Figure S7), suggesting our time series fit a linear velocity fairly well. We obtained Eurasia plate motion

velocities at 1 km spacing (Fig. 2b) (Stephenson et al., 2022) in ITRF2014 reference frame using the UNAVCO plate motion calculator and removed them from the LiCSBAS velocities. Application of this correction makes the strike-slip motion along the ATF clearer (Fig. 2c) when compared to the original LOS velocities (Fig. 2a).

3.3. Velocity field inversion and decomposition

We derived reference frame adjustment parameters for each frame using VELMAP (Wang and Wright, 2012; Wang et al., 2019) (see Text S1, Figure S9 – S12) to tie all the LOS velocity maps to the same Eurasian reference system as the GNSS data. During the VELMAP inversion, we solved for a first-order polynomial ramp related to reference frame adjustment parameters (Fig. 2d) and a linear function of topography accounting for the elevation-correlated atmospheric delay (Fig. 2e) for each InSAR frame, and then removed them from original InSAR LOS velocities to obtain the final mosaics of ascending and descending LOS velocities (Fig. 3). The residuals between the final mosaics of LOS velocities and the LOS velocity field models from VELMAP (Figure S13) do not show significant long-wavelength biases (Figure S14).

We decomposed the final LOS velocity field accounting for the local radar incidence and azimuth angle. We inverted for the east (V_e) and

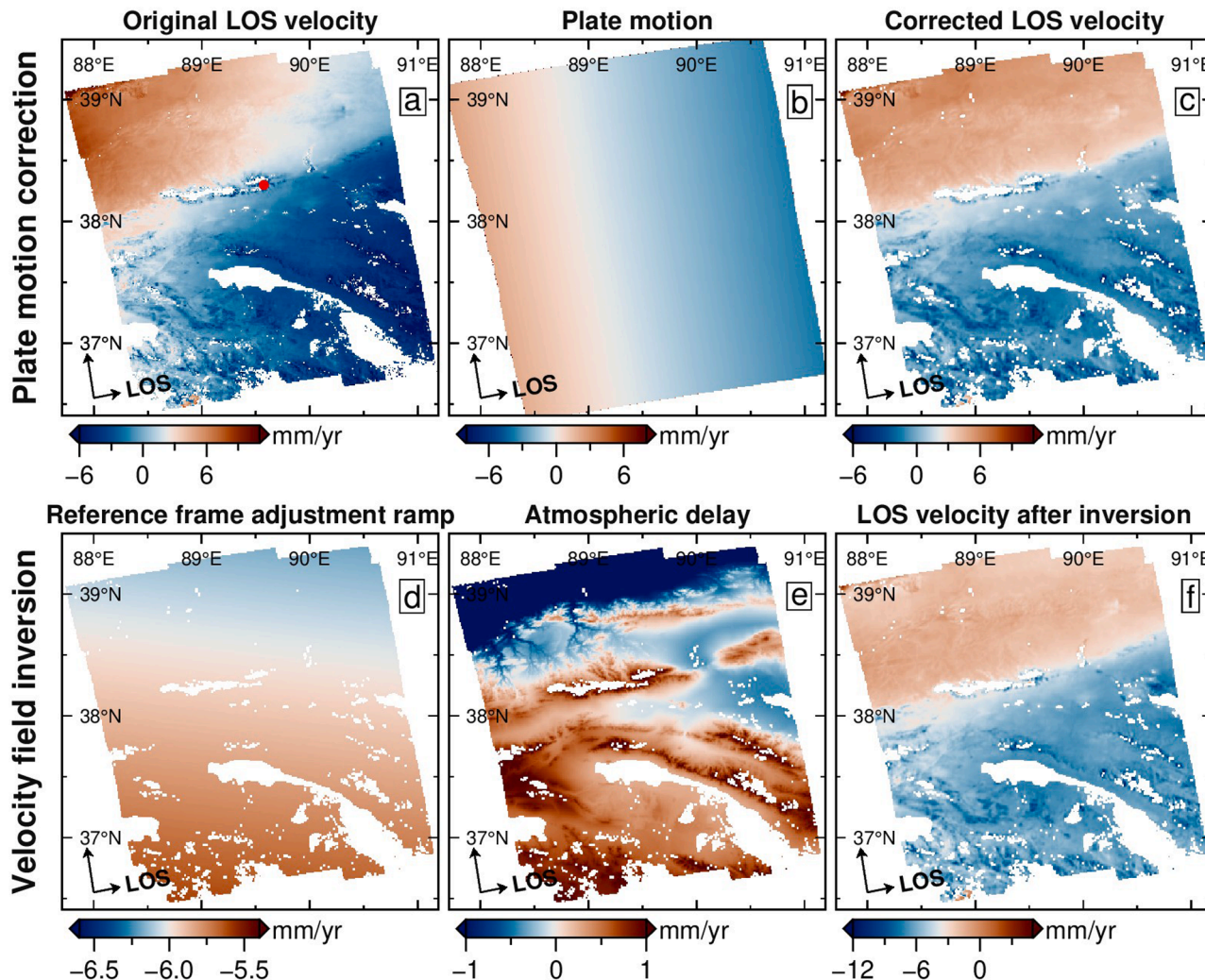


Fig. 2. Maps of InSAR processing steps for an example frame 041A_05206_161616 (covering the central portion of the ATF and Altun Shan). (a) Original LOS velocities from LiCSBAS. The red point shows the location of the time series in Figure S8. (b) LOS velocities estimated due to plate motion. (c) Corrected LOS velocities after removing the LOS velocities due to plate motion from the original LOS velocities. (d) First-order polynomial ramp related to reference frame adjustment parameters from VELMAP. (e) Elevation-correlated atmospheric delay estimated from VELMAP. (f) LOS velocities after removing the ramps related to reference frame parameters and elevation-correlated atmospheric delay from the LOS velocities after plate motion correction.

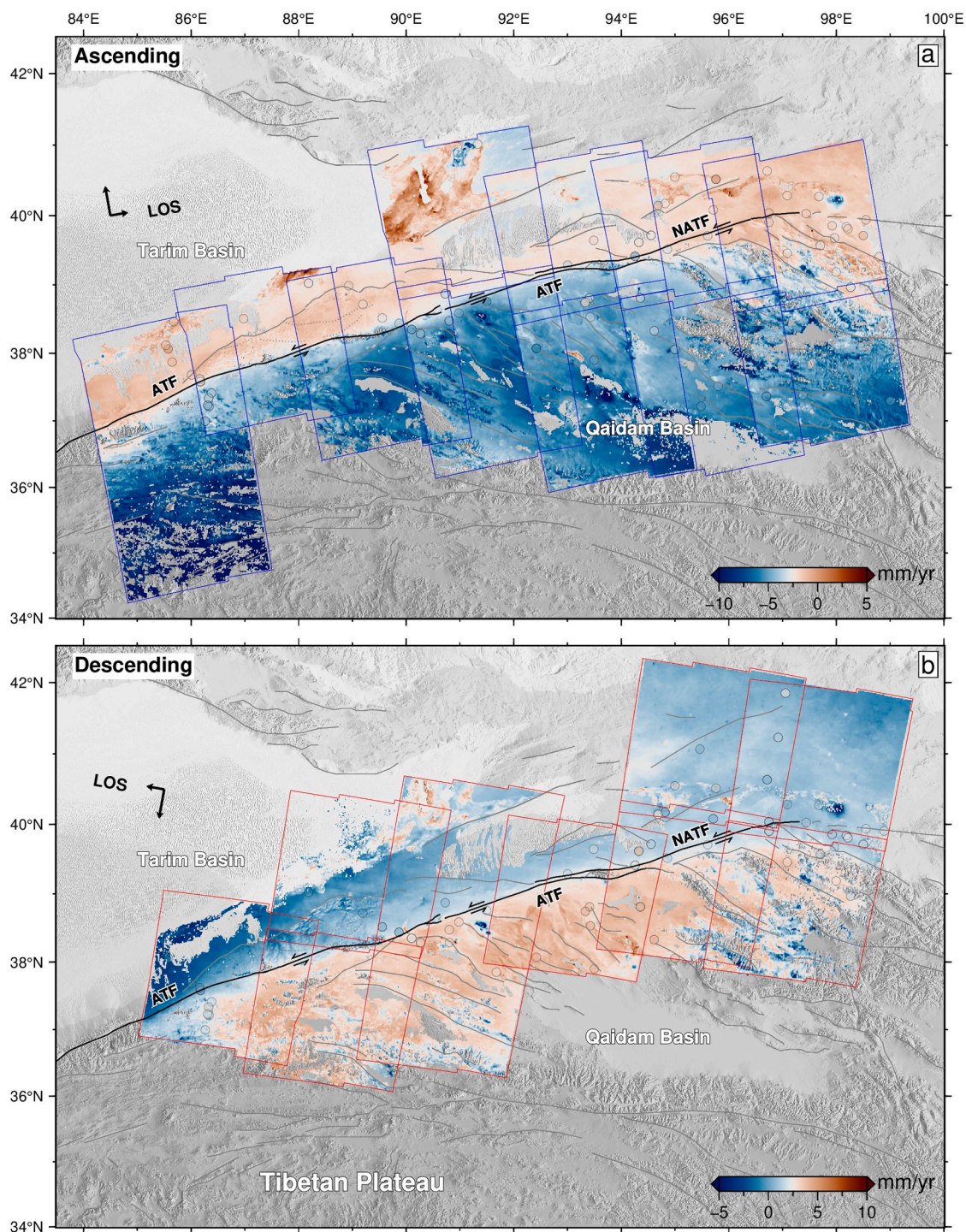


Fig. 3. Mosaics of Eurasia referenced InSAR LOS velocities based on our VELMAP inversion presented at 1 km resolution. (a) Ascending LOS velocities. (b) Descending LOS velocities. Positive values (red) indicate motion towards the satellite, while negative values (blue) indicate motion away from the satellite. Circles show the GNSS velocities projected to the same LOS directions as local InSAR rates, and the statistics of the residuals between InSAR and GNSS LOS velocities are shown in Fig. S15.

vertical velocity (V_v) (Fig. 4), as well as their associated uncertainties (Figure S16), for each pixel based on a method (Weiss et al., 2020; Watson et al., 2022) in which the solution of north velocities (Figure S11a & S12a) from the VELMAP inversion was projected in local LOS direction and subtracted from the original LOS velocities first. The remaining LOS velocities were then assumed to contain negligible long-wavelength northward component and were decomposed into V_e and V_v using weighted least squares and the variance-covariance matrix

of data.

3.4. Strain rate calculation

To capture the sharpness of the strain field and localize the concentration of deformation better, we apply the method from Ou et al. (2022), in which the horizontal strain rates are calculated based on the median filtered east velocities at the InSAR resolution and interpolated

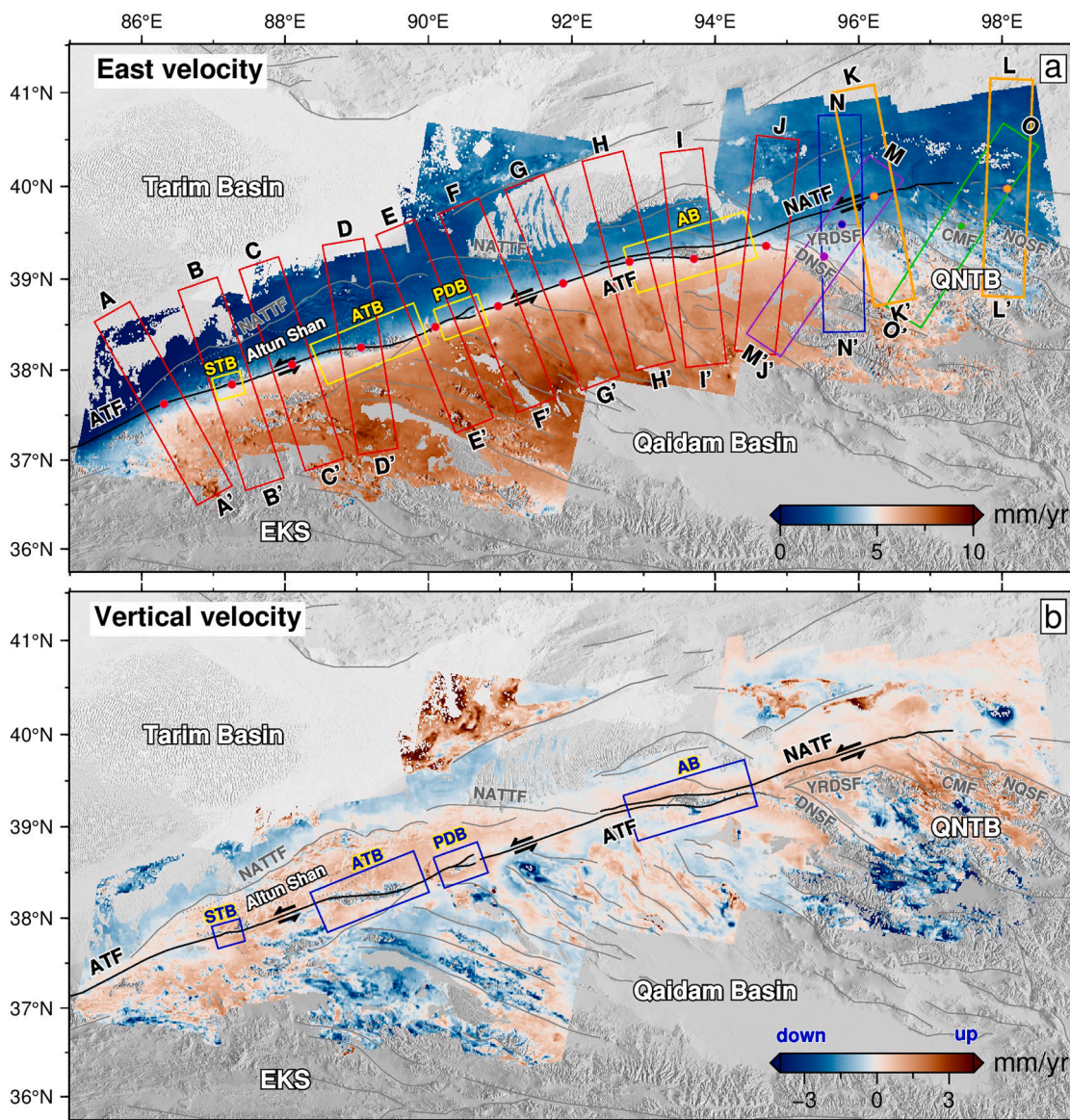


Fig. 4. Results of velocity decomposition. (a) East velocities after decomposition. The red, orange, purple, blue, and green rectangles are velocity profiles across the ATF, NATF, DNSF, YRDSF, and CMF, respectively. All the profiles are used in the following Bayesian inversion. Circles (colored by fault) represent the central locations of velocity profiles. Yellow rectangles show the spatial extent of the active bends. (b) Vertical velocities after decomposition. Blue rectangles represent the spatial extent of the active bends. Comparison between decomposed velocities and GNSS velocities is shown in Figure S17. Abbreviations are explained in the caption of Fig. 1.

north velocities from GNSS (the north velocities from VELMAP in this study). We tested the features of the strain rates observable with different window sizes (Figure S18) and found that one of 60×60 km extent can suppress the noise in the velocity field well, whilst at the same time preserving the strain rates along the main fault, which is consistent with previous tests (Ou et al., 2022). Moreover, the residuals between the original east velocities and our preferred filtered east velocities do not show significant tectonic signals (Figure S19), indicating the majority of tectonic motion has been retained within the results. We then obtain our strain rate maps (Fig. 5) using the gradients of velocities (Text S2 & Figure S20). To test the degree to which the selected smoothing factor used during VELMAP inversion will affect our strain rate model, we derive our strain rate models under three different smoothing factors (Fig. S21) and the results show that the main features of our strain rate model are insensitive to the tested range of smoothing factors used during VELMAP inversion.

4. Results

4.1. Geodetic velocity fields

The high velocity gradients along the ATF are the main feature of the LOS velocity fields (Fig. 3), seen more clearly in the East component (Fig. 4a). The sharp change closely follows the mapped ATF, confirming the dominant tectonic activity in the region is the left-lateral strike-slip movement corresponding to the deep part (below the seismogenic depth) of the ATF. The high velocity gradients along the ATF gradually disappear east of 95°E in both the LOS velocity fields and East velocity field.

The vertical velocities show long-wavelength uplifts of 1–3 mm/yr at the East Kunlun Shan range, Altun Shan range, Qaidam basin, Qilian Shan-Nan Shan thrust belt (QNTB) and active bends along the ATF (Fig. 4b), which may be controlled by tectonic activity. For example, the hypothesis that the Altun Shan range is a pop-up structure generated by

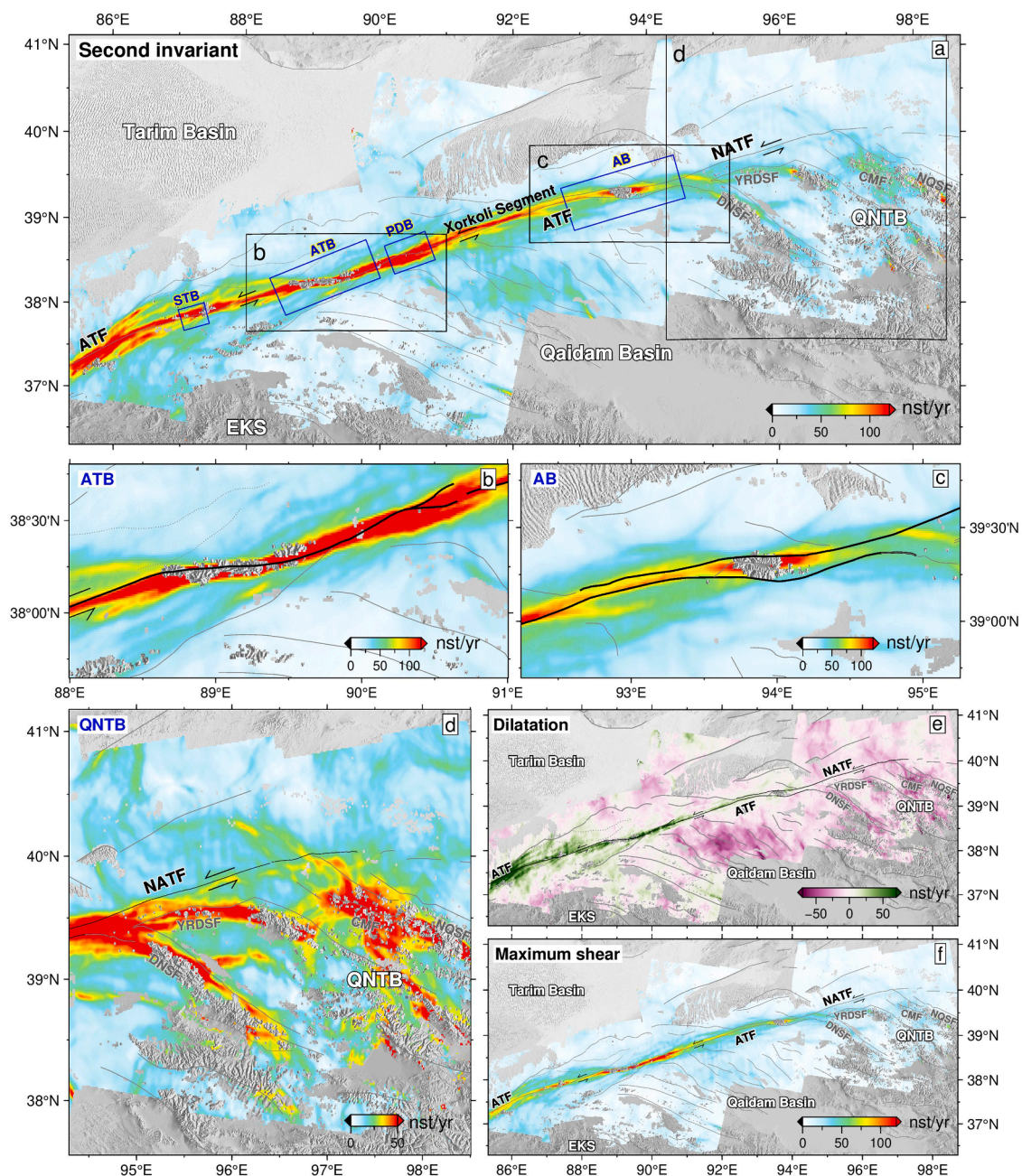


Fig. 5. Maps of horizontal strain rates from our filtered east velocity field (Figure S19a) and smooth north velocity field from VELMAP (Figure S11a). (a) Second invariant of the strain rate tensor. (b), (c) and (d) are detail maps of second invariant rates around the Akato Tagh bend (ATB), Aksay bend (AB) and Qilian Shan – Nan Shan thrust belt (QNTB), respectively. (e) Dilatation rate. (f) Maximum shear. Abbreviations are explained in the caption of Fig. 1.

extrusion of upper crustal material along the north Altyn Tagh thrust fault and other secondary faults within the range (Wu et al., 2024) provides a possible tectonic explanation for the widely distributed uplift within the Altun Shan range. Areas of subsidence as recorded in the vertical field are mostly short-wavelength signals. Such subsidence regions are likely related to small earthquakes and non-tectonic reasons such as permafrost (distributed along mountain tops) (Gruber, 2012) (Fig. S22 & S23), hydrology and anthropogenic activity. Any remaining phase bias (Ansari et al., 2021) also maps primarily into the vertical velocities.

4.2. Strain rate fields

The second invariant of the strain rate tensor (Fig. 5a & S24) shows

high strain rates over 80 nst/yr are only localized on the ATF, indicating that most of the crustal deformation in this region is concentrated on this major fault. These high strain rates (over 80 nst/yr) correlate well with the surface fault trace of the ATF. Because interseismic deformation maps the motion of the deep part of the fault beneath the seismogenic depth, this suggests that the fault planes of the ATF are near vertical. High strain rates on the ATF show obvious trend changes when crossing the Akato Tagh bend (Fig. 5b) and Aksay bend (Fig. 5c), indicating the locations of the deeper parts of the ATF are influenced by the fault bends. Narrower zones of high strain rates (over 150 nst/yr) are also observed along the Akato Tagh bend and Pingding Shan bend (Fig. 5a, b & f), suggesting shallow locking depths or shallow creep along the bends; we test this later (Section 5). The masked strain rate maps (Figure S24) also show an obvious change in the cross-fault extent of

deformation along the ATF, from which we estimate the width of the interseismic straining zone at the surface (Figure S26-S28). The surface width of this straining zone may reflect the varying locking depth, width of the shear zone at depth, or contributions from multiple faults; we found the width becomes narrower along fault bends and shows an obvious asymmetry at $\sim 88^\circ\text{E}$ (wider on the northern side) and 91.5°E (wider on the southern side) (Figure S26-S28), which may be due to the formation of fault branches near the ATF.

Two further important features can also be observed in the strain rate fields. One is the relatively high strain rates over 20 nst/yr in the Qaidam basin (Fig. 5a & S24), which do not show significant linear features and are widely distributed inside the basin, suggesting the existence of widely distributed crustal deformation across this area. Another is that

high strain rates on the ATF decrease markedly and are split into three parts at $\sim 95^\circ\text{E}$ (Fig. 5d), with most of the strain localized on the Danghe Nanshan fault (DNSF) and Yema River-Daxue Shan fault (YRDSF) and relatively low strain on the north ATF (NATF). The relatively high strain rates of ~ 50 nst/yr on the YRDSF suddenly stop in the middle of the QNTB, continued by relatively high strain rates of ~ 50 nst/yr on the Changma fault (CMF).

The dilatation rate map (Fig. 5e) indicates most areas either side of the ATF are experiencing contraction, and by masking all rates over -25 nst/yr (Figure S25), we can see that regions of high contraction are focused on the Qaidam Basin and the active fault zones in the QNTB, especially the DNSF and CMF. Short-wavelength extension signals in our dilatation map for the western portion of the ATF are potentially

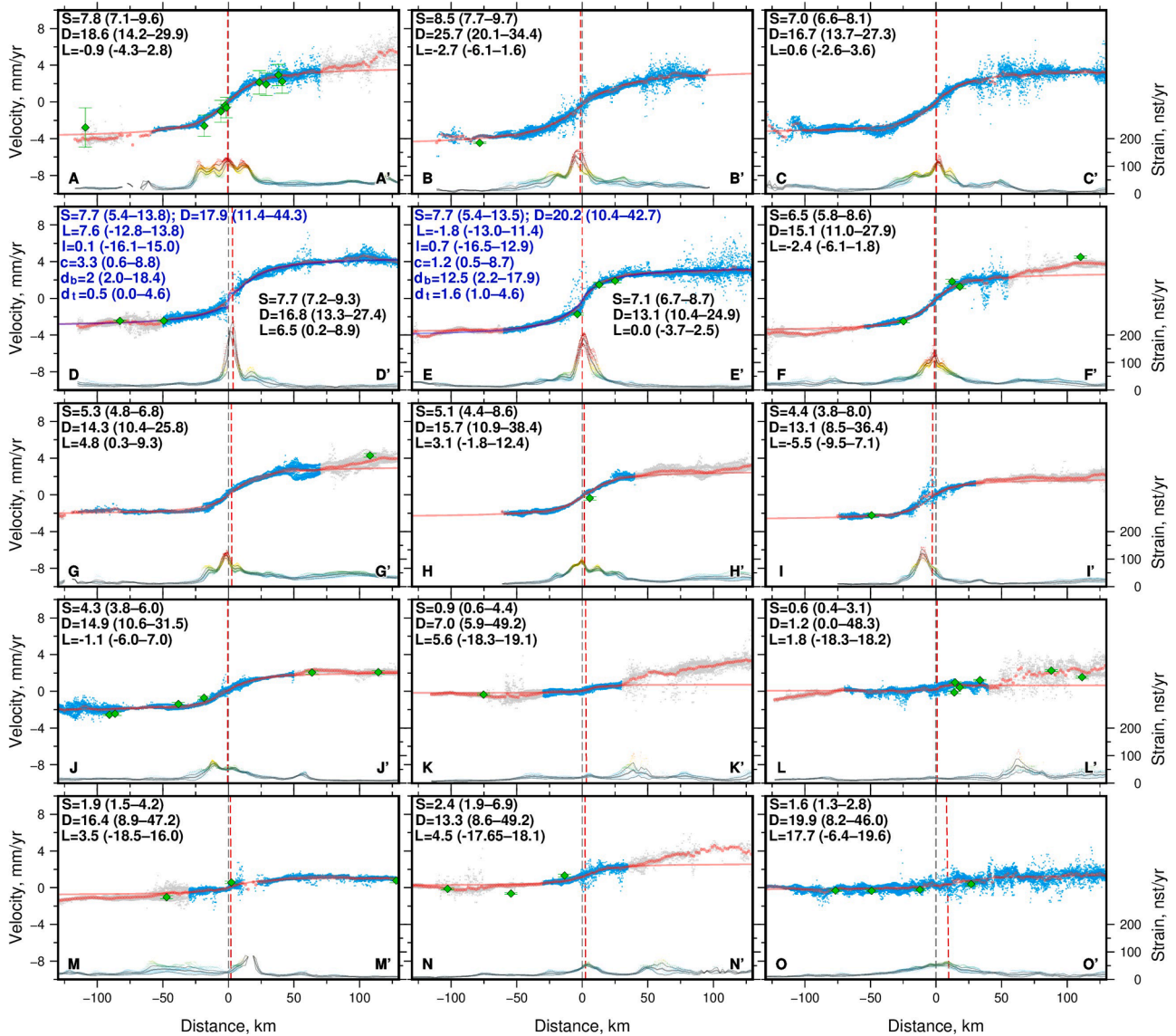


Fig. 6. Fault-perpendicular profiles of fault-parallel velocities with modeling results. The locations of the profiles are shown in Fig. 4a. Blue and gray points represent fault-parallel velocities used and omitted in modeling, respectively. Red points are binned average values for every 2 km along the profile. Red (blue) solid lines are the maximum a posteriori probability (MAP) solutions for each profile from Bayesian inversion without (with) creep components. The bottom of each plot is the second invariant strain rates (Fig. 5a) for each profile based on the same color bar used in Fig. 5a. The average and average $\pm 1\sigma$ of strain rates based on every 2-km-long bin along the profile are also showed in the plots. Vertical black dashed lines indicate the locations of mapped fault traces. Vertical red dashed lines show the MAP fault locations based on Bayesian inversion without creep components. Green diamonds are GNSS velocities and their uncertainties projected to the fault-parallel directions. Black (blue) texts are the MAP solutions and uncertainties from Bayesian inversion without (with) creep components. The uncertainties are calculated using the 2.5th and 97.5th percentiles of the recorded valid models for each parameter. If the MAP solution is less than the 2.5th percentile, a value of zero is used as the lower bound. *S*, *D* and *L* are slip rate [mm/yr], locking depth [km] and fault location [km], respectively. *c* is the shallow creep rate [mm/yr], *d_b* and *d_t* are the bottom depth [km] and top depth [km] of shallow creep, respectively. *l* is the horizontal offset [km] of creep location due to the dip angle of the fault.

artefacts due to the low sensitivity in our north component of the velocity field which may underestimate the northward compression on the ATF.

5. Analysis of fault kinematic parameters

We extracted 15 fault-perpendicular profiles (260 km long and 50 km wide) of fault-parallel velocities (Fig. 4a) and modeled them using a simple elastic dislocation model (Savage and Burford, 1973) defined by the following equations:

$$V_{para}(x) = \left(\frac{S}{\pi}\right) \arctan\left(\frac{x-L}{D}\right) + a \quad (1)$$

Where $V_{para}(x)$ is the horizontal velocities parallel to the fault, x is the perpendicular distance from the fault, S , D , L and a are the slip rate,

locking depth, fault location and scalar offset, respectively, which are unknown parameters we wanted to solve for.

For two velocity profiles (D-D' & E-E') which may include creeping signals indicated by high strain rate, we chose additional terms in the original dislocation model and also modeled the velocity profile using the following equation (Qiao and Zhou, 2021):

$$V_{para}(x) = \left(\frac{S}{\pi}\right) \arctan\left(\frac{x-L}{D}\right) - \left(\frac{c}{\pi}\right) \arctan\left(\frac{x-l}{d_b}\right) + \left(\frac{c}{\pi}\right) \arctan\left(\frac{x-l}{d_t}\right) + a \quad (2)$$

where c is the shallow creep rate, d_b and d_t are the bottom depth and top depth of shallow creep, respectively and l is the horizontal offset of shallow creep due to the dip angle of the fault.

To avoid the influence of nearby active faults, we studied the ve-

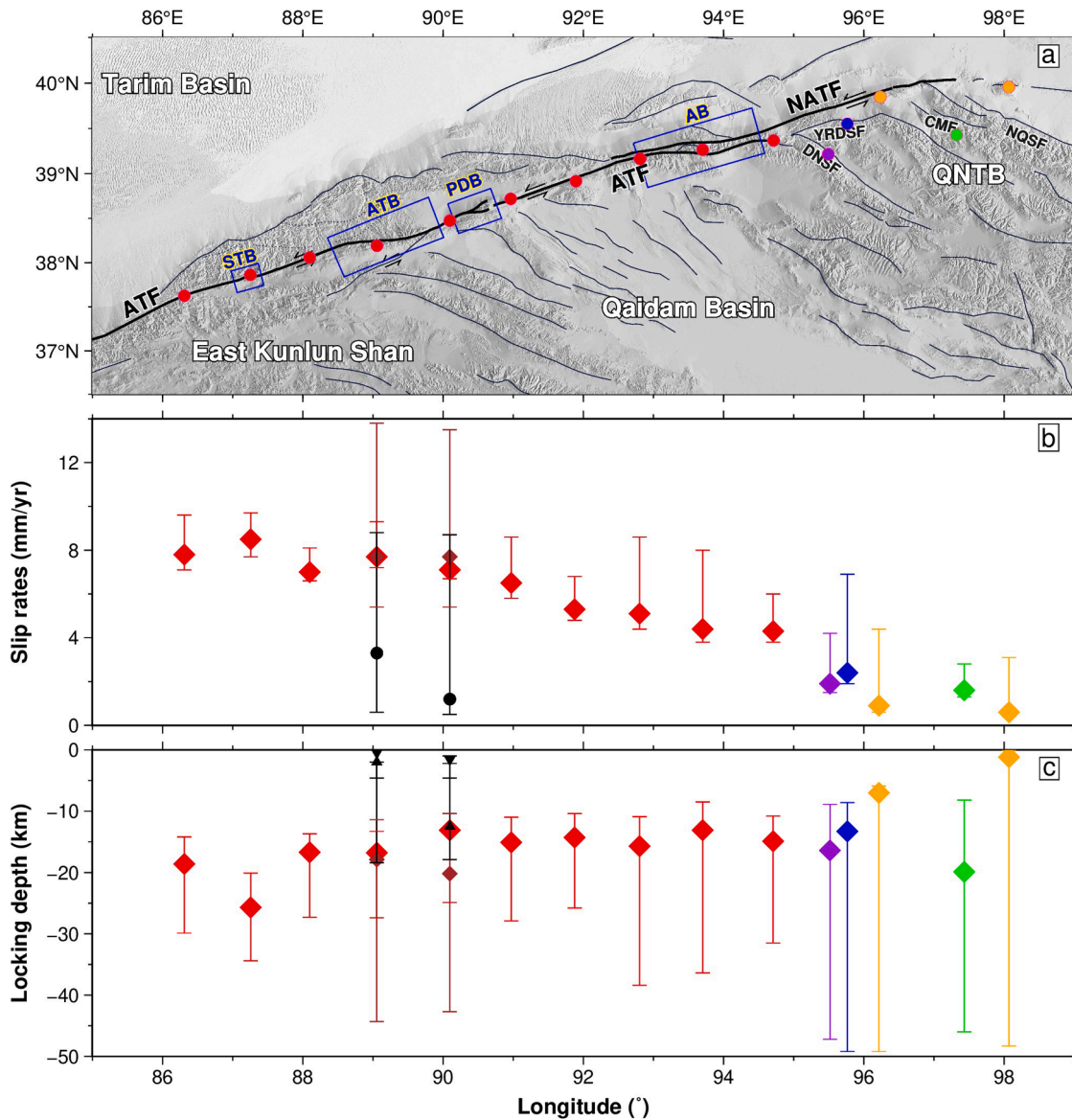


Fig. 7. (a) Comparison of fault surface traces with our MAP estimates of fault locations from Bayesian inversion. (b) Spatial variation of slip rates and shallow creep rates derived from the Bayesian inversion. (c) Spatial variation of our modeled locking depths and creep depths. Red, orange, purple, blue, and green colors are used to represent our estimates on the ATF, NATF, DNSF, YRDSF, and CMF, respectively, from Bayesian inversion without creep components. The brown diamonds in (b) and (c) represent our additional estimates of slip rates and locking depths, respectively, on the ATF from Bayesian inversion with creep components. Black circles in (b) are our modeled creep rates from Bayesian inversion with creep components. Black triangles and inverted triangles in (c) correspond to bottom and top depths of creep, respectively, from Bayesian inversion with creep components. Abbreviations are explained in the caption of Fig. 1. The method for estimating uncertainties is described in the caption of Fig. 6.

locities and strain rates in the profiles and then masked some parts of the velocity profiles when we found there was a sudden change in velocity pattern or a sudden increasing of strain rates far away from the main fault traces (Fig. 6). The masked velocity profiles were used to find the best-fitting model parameters based on a Bayesian approach (Watson et al., 2022), which uses an affine-invariant ensemble Markov Chain Monte Carlo sampler (Goodman and Weare, 2010) to explore parameter space and estimate both the maximum a posteriori probability (MAP) solution and corresponding parameter uncertainties. Uniform prior for all model parameters was assumed in the modeling, and for velocity profiles without creeping signals, we used limits of $0 \leq S \leq 20$ (mm/yr), $0 \leq D \leq 50$ (km), $-20 \leq L \leq 20$ (km) and $-10 \leq a \leq 10$ (mm/yr) for the parameters. For profile DD' and EE' where the strain rate maps (Fig. 5a, b & f) suggest there are potential creeping signals, we used additional limits of $0 \leq c \leq 10$ (mm/yr), $0 \leq d_b \leq 20$ (km), $0 \leq d_t \leq 5$ (km) and $-10 \leq l \leq 10$ (km) for related parameters. We used 400 walkers (or chains) in the modeling, and for each walker we generated 500 iterations and then removed the first 20% of iterations as burn in (the initialization phase before the stabilization phase in parameter convergence), which means that the total number of valid models is 160,000 and the total number of iterations in the modeling is 200,000. During the modeling, we use a further variance-covariance matrix to account for the spatial correlation of noise so that the misfit of model solutions is better weighted (Hussain et al., 2016; Watson et al., 2022) (Text S3).

The modeling results and their uncertainties for each profile are shown in Fig. 6, and the marginal probability distribution of each profile can be found in Figures S29–S45. Overall, because of the high sensitivity of InSAR to eastward motion and the low level of noise in our average velocities from a long time series of observation dates, the strike-slip rates are well constrained in our results. We see that the strike-slip motion on the ATF is relatively stable between 86°E and 90.5°E (Fig. 7), with consistent MAP strike-slip rates of ~8 mm/yr. Between 90.5°E and 94°E, the ATF slip rate shows a gradual decrease of ~3 mm/yr, and then, east of 94°E, the strike-slip motion of 4.3 (3.8–6.0) mm/yr on the ATF which at ~95°E transfers to strike-slip motion of 1.9 (1.5–4.2) mm/yr along DNSF, 2.4 (1.9–6.9) mm/yr along the YRDSF and 0.9 (0.6–4.4) mm/yr along the NATF. The CMF also shows a strike-slip motion of 1.6 (1.3–2.8) mm/yr. We find MAP estimates for locking depth across most profiles are 15 ± 5 km, which is consistent with the estimation in most previous studies (e.g., Liu et al., 2018). For profiles such as KK' and LL', the strike-slip motion on the NATF is very weak compared to the noise in the velocities, resulting in a small locking depth with a large uncertainty.

We test models with or without creep components for profile DD' and EE' (Text S4, Figure S46), and the results show that both models can fit the input velocities similarly well. For profile DD', confirmation of shallow creep is difficult due to missing data around the surface fault trace, while for profile EE', the results show adding a creep component to the model can better fit the high strain rates (>200 nst/yr) and narrow width of high straining zone.

We also test the block rotation effects within the Tarim basin on our slip rate inversion (Text S5, Figure S47–S50), and the results show these effects are limited and the difference in MAP slip rates can be less than 1 mm/yr. Given the uncertainties within our data, we consider block rotation effects to be negligible.

6. Discussion

6.1. Strain features around active restraining bends

By resolving the location of the peak strain rates along the ATF, we found the trend of peak strain rates (see blue squares and numbers in Fig. 8a) changes from ~N70°E to ~N83°E when crossing the Akato Tagh bend, and similar trend changes can also be observed when crossing the Aksay bend. A trend (or strike) change of ~13° of the deep shearing part of the fault beneath the Akato Tagh bend is much smaller than the trend

change of ~20° seen in the fault surface trace (Elliott et al., 2015), which may be related to the different dipping angles of faults at two sides of the bend as our peak strain rate traces (Fig. 5b & 8a) shows that the deeper extent of the fault zone is shifting to the south in the west of the Akato Tagh bend and shifting to north in the east. Studies from Cowgill et al. (2004) suggest that the Akato Tagh bend should undergo vertical-axis rotation if the shortening across the bend is mainly focused in the two inside corners. Profiles of vertical velocities across the Akato Tagh bend show that uplift rate is ~0.5 mm/yr averaged around the bend and becomes larger to over 1 mm/yr at the inside corner of the bend (Fig. 8e). This suggests the largest shortening happens within the inside corners of the bend, which is consistent with the hypothesis of vertical-axis rotation. In addition, we observe a smaller strike change in the deep shearing part of the fault compared to the fault surface traces. This suggests the vertical-axis rotation is driven by the shearing part in the deep crust. A special feature of Akato Tagh bend is the relatively high strain rates at the southern side of the bend (Fig. 5b, 8a & S24), suggesting active branches (e.g. the Baiganghu fault (Liu et al., 2017)) may form in the southern borderland of this restraining bend. The trace of peak strain rates around the Aksay bend (Fig. 5c & 8a) indicates that the underlying fault plane might pass through the middle of this bend, which is consistent with the results from magnetotelluric data (Xiao et al., 2017).

All the major restraining bends show higher peak strain rates and a narrower width (~20 km) of the interseismic straining zone at the surface (Fig. 8b & c), especially the Akato Tagh bend and Pingding Shan bend, along which the magnitudes of peak strain rates are near double that of the straight segments such as the Xorkoli segment (Fig. 8b). These strain concentrations and high velocity gradients leave open the possibility of shallow creep along these sections based on our modeling, but large uncertainties cannot make this definitive without further work (Text S4). Shallow creep near fault discontinuities like pull-apart basins or fault bends have been observed along several large-scale strike-slip faults, such as the Haiyuan fault (Jolivet et al., 2013) and the Xianshuihe fault (Qiao and Zhou, 2021), and the creep sections are normally accompanied by a strong micro- and moderate seismic activity (Jolivet et al., 2013). The ATF may show similar patterns, as the majority of recent earthquakes occur near the Akato Tagh bend and Pingding Shan bend, while the Xorkoli segment remains relatively silent (Fig. 1a). Previous studies have shown that historic seismic ruptures found on the Xorkoli segment can be halted by the restraining bends along the ATF (Elliott et al., 2015; Shao et al., 2018); shallow creep may relieve some of the tectonic strain aseismically (Harris, 2017), although the current creeping rates may also have been influenced by recent earthquakes near to the bends. We note, however, the continuity and relative smoothness of the deep shear zone means that through-going ruptures cannot be ruled out. Supershear ruptures have been observed on several large-scale strike-slip faults, and studies show that they are more likely to occur on faults with simple geometry (Bruhat et al., 2016). We consider the straight fault segment with a continuous and relatively straight fault plane in the deep crust between the Pingding Shan bend and Aksay bend may have the potential to generate supershear earthquakes along the central ATF, an area with over 300 years absence of a historic earthquake (Yuan et al., 2020).

All the restraining bends are uplifting in their borderland except for some short-wavelength subsidences related to permafrost or landslides (Fig. 8d). The uplift rate becomes larger at the inside corner of the bends (Fig. 8e–g), suggesting there is strong compression near these restraining bends causing regional crustal shortening. This strong compression may result in earthquakes with both strike-slip and thrust components, such as the 1993 Mw 6.2 earthquake (Fig. 1a).

6.2. Evidence supporting eastward gradual decrease in slip rate and slip partitioning

In the pattern of slip rates proposed by Liu et al. (2020) based on

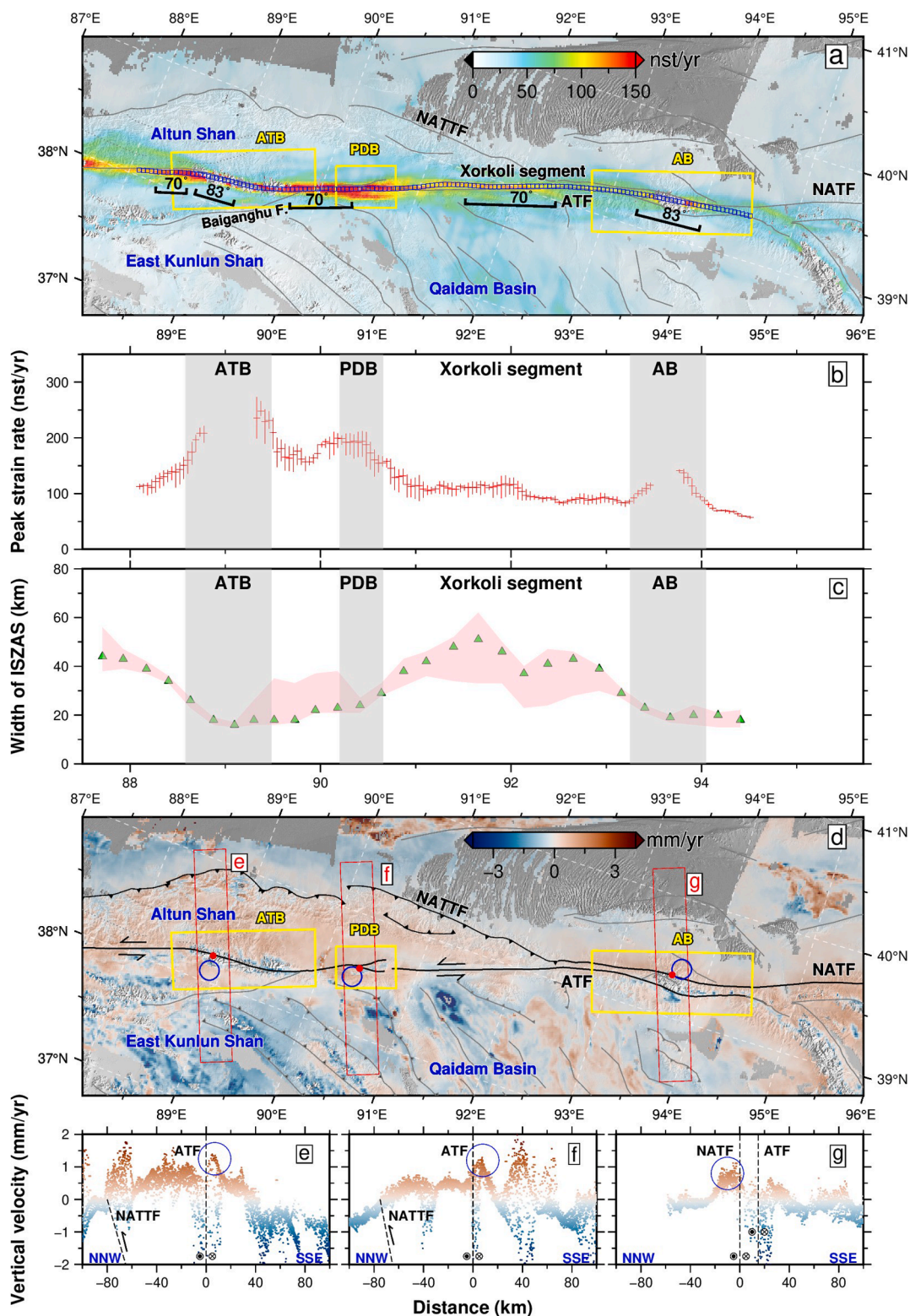


Fig. 8. Strain rate distribution and vertical velocity field around major active restraining bends along the central Altyn Tagh fault (ATF). (a) Second invariant strain rates. The angles represent the strike directions of the ATF indicated by the orientation of peak strain rates. The spatial extent of the segments used for these angle estimates is shown below the numbers. Blue squares of 4 km × 4 km extent along the ATF denote the location of peak strain rates. Yellow rectangles show the spatial extent of the active bends. (b) Peak strain rates derived from the rates in the blue squares in (a). Horizontal lines represent the average rates in each square. End points of vertical lines represent the maximum and minimum rates in each square. (c) Spatial variation of the width of the interseismic straining zone at the surface (ISZAS) estimated by second invariant rate maps (see Figure S26–28). Green triangles represent widths of ISZAS measured from the map of second invariant rate over 45 nst/yr, while upper and lower boundary of the pink shaded band show widths of ISZAS estimated from maps of second invariant rate over 40 and 50 nst/yr, respectively. (d) Vertical velocity field. Yellow rectangles show the spatial extent of the active bends. Blue circles represent the locations of the inside corners of fault bends. (e), (f) and (g) are vertical velocity profiles based on the polygons in (d). The zero value in horizontal axis represents the location of red points in (d). Blue circles highlight the uplift signals within the inside corners of fault bends.

study of Late Quaternary offsets, a constant long-term slip rate of ~ 10 mm/yr is thought to exist between 86°E and 94°E , with this decreasing sharply to ~ 5 mm/yr at 95°E . Such a pattern is consistent with high slip rates found near 94°E in several studies (e.g. Zhang et al., 2007; Jolivet et al., 2008) (Fig. 9), but a lack of change in slip rate between 86°E and 94°E would not be consistent with the crustal shortening in the Qaidam basin indicated by other research (e.g. Zhou et al., 2006; Yin, et al., 2008; Guo et al., 2017) and also the high seismicity inside the Qaidam basin. Another pattern proposed by Li et al. (2018) based on elastic block modeling of GNSS data considers the slip rate decreasing gradually from 11 mm/yr to 6.2 mm/yr between 85°E to 94°E and then more sharply reducing between 94°E and 95.5°E . This pattern gives a relatively low slip rate at 94°E and supports a decrease of fault slip rates to the west of 94°E , but due to the low spatial resolution of GNSS data, greater detail of the spatial variation of slip rates could not be revealed. In this study, we are able to determine the spatial variation of slip rates between 86°E to 95°E for the ATF (Fig. 9). Our slip rate estimates are stable at ~ 8 mm/yr between 86°E and 90.5°E , then gradually decrease to ~ 4.5 mm/yr at 94°E . Our derived slip rates are approximately constant between 94°E and 95°E , rather than decreasing sharply.

Our results also illustrate how slip rates transfer and decrease east of 95°E (Fig. 9). Previous geodetic slip rates on the eastern part of the ATF are mostly from GNSS and because of the low spatial resolution of such data, the big assumption implicit in these results is that the strain is mainly accumulated along the northern ATF (NATF). Based on this assumption, 4–5 mm/yr slip rates were reported at 95°E to 96°E (Zhang et al., 2007; Zheng et al., 2017; Li et al., 2018). From our strain rate and

modeling results, we suggest the GNSS velocities fail to correctly identify the location of the sources of the strain and instead overestimate the slip rates on the NATF. Our modeling results show the slip rate on the NATF at 96°E is only ~ 1 mm/yr and most strike-slip motion on the ATF has by this longitude transferred instead onto the DNSF and YRDSF (Fig. 9), with a rate of 1.9 (1.5–4.2) mm/yr and 2.4 (1.9–6.9) mm/yr, respectively. A slip rate of 0.9 (0.6–4.4) mm/yr on the NATF at 96°E is consistent with recent geological estimates of 1.2 ± 0.1 mm/yr measured by high-resolution topographic data and optically stimulated luminescence dating methods (Yan et al., 2024) (Fig. 9). The slip rate of 2.4 (1.9–6.9) mm/yr we found for the YRDSF is also consistent with results from Luo et al. (2015) based on offsets of river risers and gullies, which show the slip rate on this fault since the late Pleistocene is 2.8 ± 0.3 mm/yr. For the eastern end of the NATF at 98°E , we estimated a slip rate of 0.6 (0.4–3.1) mm/yr, which is consistent with the slip rates of 0.6 ± 0.2 derived from Quaternary offset dating (Yang et al., 2023) (Fig. 9), suggesting that the strike-slip motion on the NATF may extend to a more eastern location. We find a strike-slip rate of 1.6 (1.3–2.8) mm/yr on the CMF, which produced the 1932 Ms 7.6 Changma earthquake (Fig. 1a); this rate is lower than the 4 mm/yr estimated from previous geological data (Du et al., 2020).

6.3. Interpretation of spatial variation of fault slip rates, mountain building and fault termination

We extract fault-parallel velocities of InSAR and GNSS in a Eurasia reference frame based on two 100-km-wide fault-parallel swath profiles

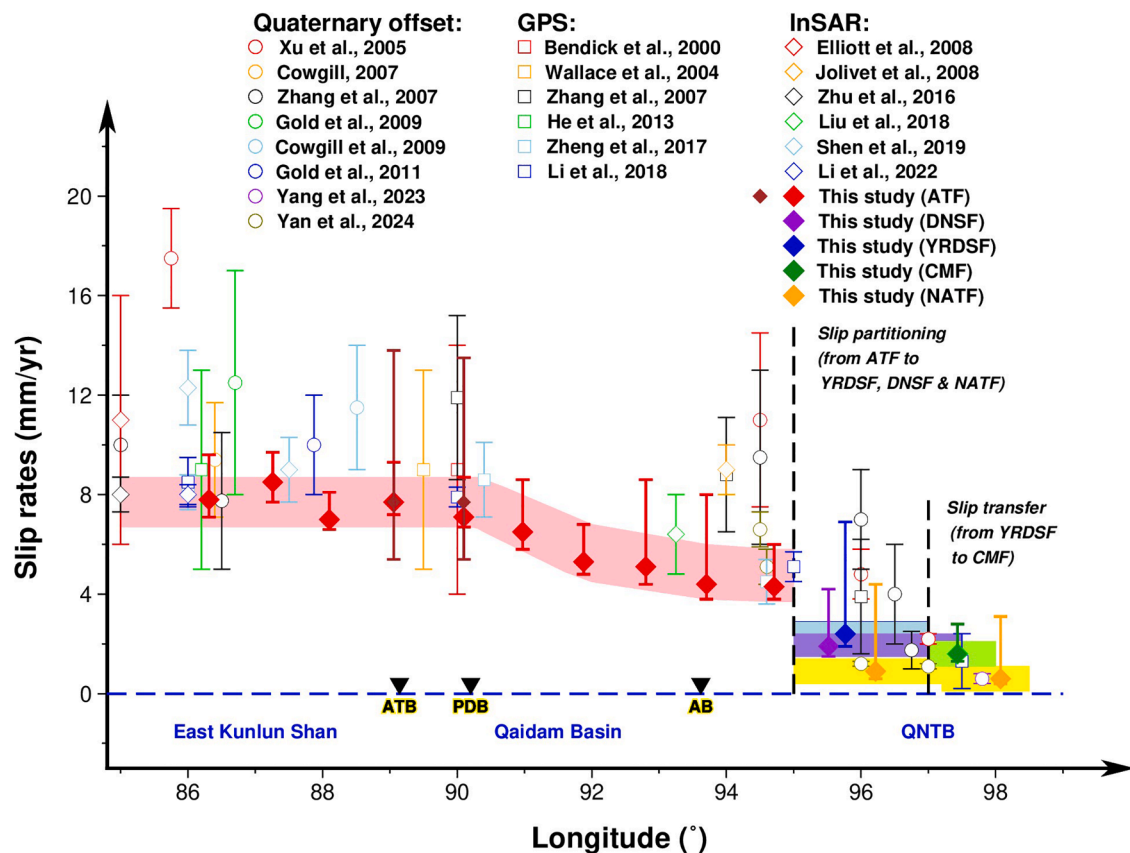


Fig. 9. Spatial distribution of slip rates along the central-eastern Altyn Tagh fault system estimated here and compared to previous published studies. The red, orange, purple, blue, and green diamonds (filled with the same color) are our modeled slip rates on the ATF, NATF, DNSF, YRDSF, and CMF, respectively, from Bayesian inversion without creep components. The brown diamonds represent our additional estimates of slip rates on the ATF from Bayesian inversion with creep components. The pink, yellow, purple, light blue, and green shaded bands represent a possible pattern of the spatial variation and extent of the strike-slip motion on the ATF, NATF, DNSF, YRDSF, and CMF, respectively, based on our MAP slip rate estimates (the width is illustrative rather than representing the true uncertainty). Blue dashed line represents a slip rate of zero. Black triangles show the locations of active bends based on the given longitudes along the horizontal axis. Abbreviations are explained in the caption of Fig. 1.

on either side of the ATF (Fig. 10a & b). In the northern profile (PP'), velocities are relatively stable with values of $\sim 4 \pm 1$ mm/yr between 86°E and 94°E and decrease slowly to ~ 2 mm/yr from 94°E to 98°E. The southern profile (QQ') shows stable fault-parallel velocities of $\sim 10 \pm 1$ mm/yr between 86°E to 90.5°E, and an upper-bound difference of ~ 8

mm/yr for the northern and southern profiles between 86°E and 90.5°E is consistent with our stable slip rate estimates of ~ 8 mm/yr along this section of ATF. East of 90.5°E, the fault-parallel velocities in the southern profile decrease to $\sim 8 \pm 1$ mm/yr when crossing the Qaidam basin, combined with regional uplift observed inside the basin (Fig. 4b &

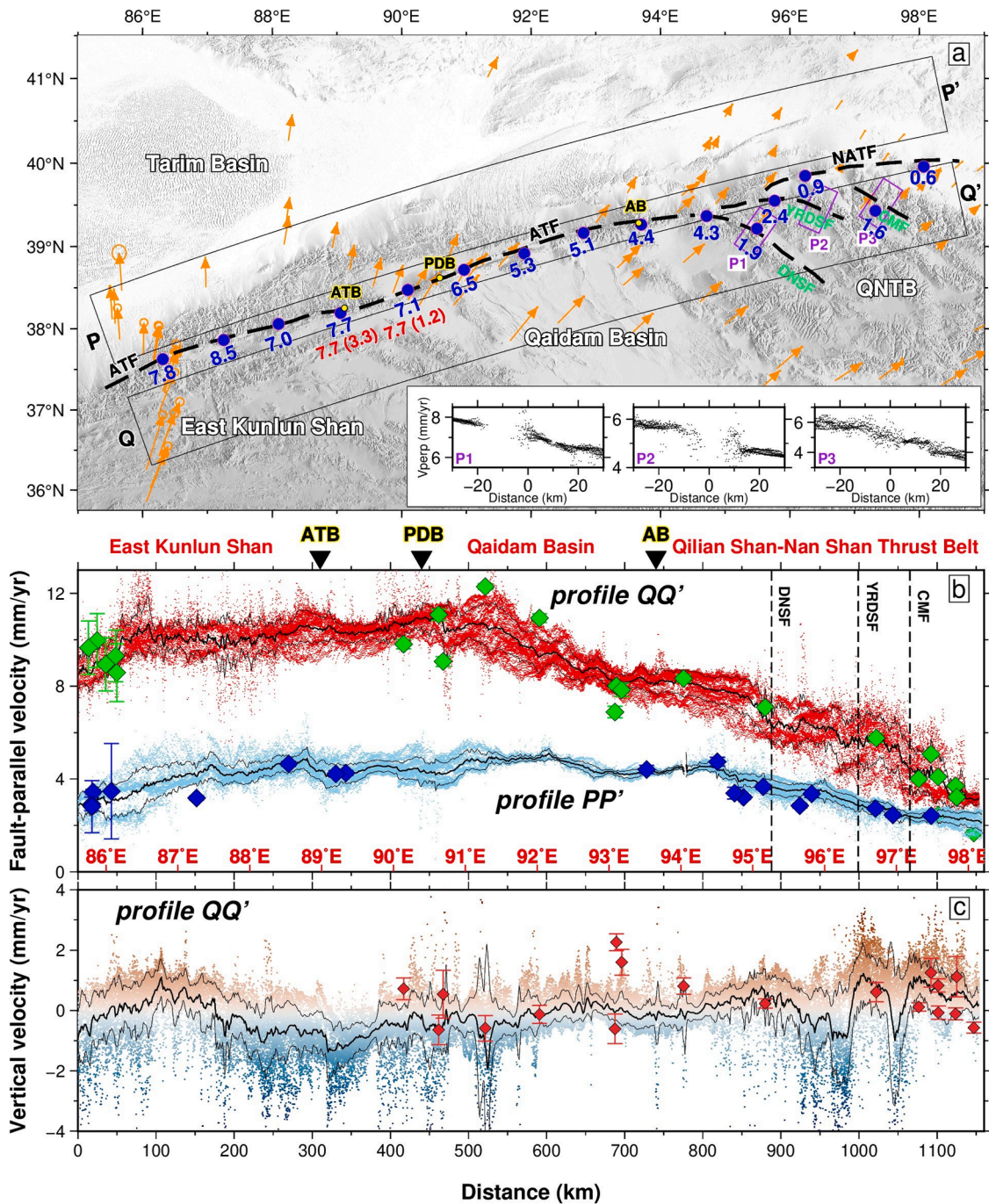


Fig. 10. Interpretation of the spatial variation of slip rates along the central-eastern Altyn Tagh fault system. (a) Spatial variation of our modeled slip rates [mm/yr]. Black dashed lines represent the fault locations indicated by the strain rate fields. Blue points show the centers of the fault based on our Bayesian inversion (without creep components) results. Blue numbers are our modeled slip rates from Bayesian inversion without creep components. Red numbers are our modeled slip rates and creep rates based on Bayesian inversion with creep components, with the creep rates shown in the brackets. The bottom-left corner are fault-perpendicular velocity profiles (from west to east) for the DNSF, YRDSF and CMF based on their strikes, and their locations have been shown using purple rectangles in (a). The size of the purple rectangles are 60 km × 30 km. (b) Fault-parallel velocity profiles for the ATF based on an average strike of N70°E. The locations of the profiles have been shown using black rectangles in (a). Black lines are binned average values and values with a difference of 1σ to the averages for every ~ 1.2 km along the profiles. Green and blue diamonds are horizontal GNSS velocities within each profile projected to the fault-parallel direction. Black dashed lines are locations of the DNSF, YRDSF and CMF. Approximate longitudes for the velocities are shown using red numbers at the bottom of the plot. (c) Vertical velocities for profile QQ' in (a). Black lines are binned average values and values with a difference of 1σ to the averages for every ~ 1.2 km along the profiles. Red diamonds are vertical GNSS velocities within the profile. Abbreviations are explained in the caption of Fig. 1.

10c), suggesting crustal shortening is happening across the Qaidam basin. This is consistent with previous geological results based on seismic sections (Zhou et al., 2006; Yin, et al., 2008) showing that the Qaidam basin has experienced continuous compression and shortening since the early Cenozoic when the ATF was formed by the India-Asia collision. The present shortening rate of the Qaidam basin in the ATF fault-parallel direction is estimated to be $\sim 2.5 \pm 1$ mm/yr from our results, which is very close to the average shortening rate since 2.8 Ma measured from cross-section restoration (Zhou et al., 2006; Guo et al., 2017). The shortening of the Qaidam basin provides a good explanation for a decrease of ~ 3 mm/yr in our slip rate estimates on the ATF between the Pingding Shan bend and Aksay bend.

Unlike the Qaidam basin where the fault-parallel velocities decrease linearly in the southern profile, the velocities in the Qilian Shan-Nan Shan thrust belt (QNTB) are more likely decreasing step-like and are dominated by the DNSF and CMF. From 60-km-long fault-perpendicular profiles of fault-perpendicular velocities across the DNSF, YRDSF and CMF (Fig. 10a), we find the total convergent rates of these fault zones are $\sim 1.5 \pm 0.2$ mm/yr, $\sim 1.2 \pm 0.3$ mm/yr, $\sim 2.2 \pm 0.7$ mm/yr, respectively. Assuming the strike direction of the DNSF and CMF is $\sim N120^\circ E$, we estimate a total decrease of ~ 5.1 (4.0–8.0) mm/yr in fault-parallel velocities (parallel to ATF) when moving across these two fault zones, which is very close to the total shortening of $\sim 5 \pm 1$ mm/yr in the QNTB we found in the southern profile (Fig. 10b), suggesting most of shortening in the QNTB is happening in active fault zones and controls the regional uplift (Fig. 10c). Q. Xu et al. (2021) also estimated the shortening rates for the DNSF, YRDSF and CMF (or Western Qilian Shan in their paper) on timescales of 10^4 – 10^5 years, and their results are $\sim 1.25 \pm 0.25$ mm/yr, $\sim 2.2 \pm 0.2$ mm/yr and $\sim 1.6 \pm 0.2$ mm/yr, respectively. They estimated a relatively larger shortening rate on the YRDSF because they assume all the strike-slip motion west of the fault is transferred into thrust motion east of it, while our velocity field shows only part of the strike-slip motion has transferred into thrust motion and then all the motion on this fault is transferred into the oblique-slip motion on the CMF at $\sim 97^\circ E$.

Based on our results, we suggest the ATF terminates in a horsetail structure east of $\sim 95^\circ E$, and this structure mainly consists of three faults, comprising the DNSF, YRDSF and NATF. Both the DNSF and YRDSF are interpreted as strike-slip faults with reverse component, and they extend eastward and finally die out in the QNTB. The eastern termination of the ATF is similar to the eastern termination of the North Anatolian fault system (Gürboğa, 2016), which also terminates in a horsetail structure. Such a terminal pattern is different from the previous termination pattern proposed by Xu et al. (2005), in which the ATF terminates by three triple junctions along the NATF. This termination of the ATF is also different from the Haiyuan fault, another intra-plate strike-slip fault at the northern edge of the Tibetan plateau, which terminates by a “seamless” transition zone at its eastern end, with strike-slip movement on the fault being transformed to the thrusting movement on the Liupanshan fault (Li et al., 2017).

6.4. Asymmetric strain

Asymmetric deformation along the ATF has been observed by several previous studies (Jolivet et al., 2008; Ge et al., 2022), and this is normally explained by contrasting rheological structure or different material stiffness either side of the fault. From our velocity and strain rate profiles across the Altun Shan range and the eastern Kunlun Shan (Fig. 6) we do not find an obvious asymmetric pattern in the data. Significant asymmetric deformation can be noticed in profiles across the Tarim basin, Altun Shan range and Qaidam basin (Profiles GG' & HH' in Fig. 6), but because significant shortening is happening within the Qaidam basin, the asymmetric pattern in the velocity profiles is more likely controlled by the secondary faults within the Qaidam basin. Jolivet et al. (2008) observed significant asymmetric strain in a velocity profile at $\sim 94^\circ E$ and suggested it may be caused by the different rigidity of the

crust in two sides of the fault. However, based on our velocity profiles close to $\sim 94^\circ E$ (Profiles II' & JJ' in Fig. 6), we do not observe significant asymmetric pattern across the fault, and we also estimated a much smaller slip rate compared with results from Jolivet et al. (2008).

7. Conclusion

We have mapped the strain accumulation along the central-eastern Altyn Tagh Fault (ATF) using a high-resolution velocity field derived from Sentinel-1 InSAR and GNSS data from which we have evaluated fault parameters such as slip rate and locking depth using a Bayesian inversion approach. Our results show that the strain is mainly focused on the ATF in northwestern Tibet, suggesting it can act as the north boundary of the Tibet deformation. The ATF shows constant strike-slip rates of ~ 8 mm/yr between $86^\circ E$ and $90.5^\circ E$, before decreasing gradually to ~ 4.5 mm/yr between $90.5^\circ E$ and $94^\circ E$ due to the crustal shortening of $\sim 2.5 \pm 1$ mm/yr across the Qaidam basin. The ATF terminates in a horsetail structure at $95^\circ E$, with strain split into motion along the Danghe Nanshan fault (DNSF), Yema River – Daxue Shan fault (YRDSF) and north ATF (NATF). The DNSF and YRDSF accommodate most of the strain and are interpreted as oblique-slip faults with strike-slip components of 1.9 (1.5–4.2) mm/yr and 2.4 (1.9–6.9) mm/yr, respectively, while the NATF accommodates little of the strain with a strike-slip rate of 0.9 (0.6–4.4) mm/yr at $\sim 96^\circ E$ and 0.6 (0.4–3.1) mm/yr at $\sim 98^\circ E$. Strain accumulation along the YRDSF suddenly stops in the middle of the Qilian Shan-Nan Shan thrust belt (QNTB) and is carried instead along the Changma fault (CMF), which is an oblique-slip fault with strike-slip components of 1.6 (1.3–2.8) mm/yr. The QNTB is in a transpressional environment, and almost all of the shortening inside it is happening across the fault zones. The fault planes beneath the ATF are near vertical with a strike change of $\sim 13^\circ$ within the deep shearing part of the fault beneath the Akato Tagh bend and Aksay bend. Obvious higher strain rates and narrower width of the interseismic straining zone at the surface along the Akato Tagh bend and Pingding Shan bend are observed in our results. The thrust motion of the active faults may control the uplift in the QNTB as obvious shortening across the active fault zones have been observed in our results. Relative larger uplift rates at the inside corners of the restraining bends provides important geodetic evidence for potential vertical-axis rotation within the bends.

CRediT authorship contribution statement

Dehua Wang: Writing – review & editing, Writing – original draft, Visualization, Validation, Software, Resources, Project administration, Methodology, Investigation, Funding acquisition, Formal analysis, Data curation. **John R. Elliott:** Writing – review & editing, Supervision, Resources, Funding acquisition, Formal analysis, Conceptualization. **Gang Zheng:** Writing – review & editing, Writing – original draft, Supervision, Resources, Funding acquisition, Formal analysis, Data curation. **Tim J. Wright:** Writing – review & editing, Supervision, Software, Resources, Conceptualization. **Andrew R. Watson:** Software. **Jack D. McGrath:** Software.

Declaration of competing interest

The authors declare that they have no known competing financial interests or personal relationships that could have appeared to influence the work reported in this paper.

Data availability

Our estimated GNSS velocities can be found in the supplementary material. The line-of-sight velocities, decomposed velocities, velocity uncertainties, and the strain rate fields we derived are preserved at doi: <https://doi.org/10.17632/78864g22zg.1>, available via the CC BY 4.0 license. The VELMAP codes can be accessed through the following link:

<https://github.com/nerc-comet/velmap>.

Acknowledgements

We thank the European Space Agency (ESA) for the open data policy on the Sentinel-1 mission. The InSAR data are copyrighted by ESA and are provided through the Copernicus Open Access Hub (<https://scihub.copernicus.eu/>). The Sentinel-1 InSAR data are also freely distributed by the Alaska Satellite Facility (<https://asf.alaska.edu/>). We are grateful to all of our Chinese colleagues who contribute to the CMONOC project. This work was supported by the China Scholarship Council-University of Leeds joint scholarship to Dehua Wang, the Royal Society grants to John Elliott (UF150282 and URF/R/211006) and Gang Zheng (NIF\R1\201854), the UK Natural Environment Research Council (NERC) through the Centre for the Observation and Modeling of Earthquakes, Volcanoes, and Tectonics (COMET, a partnership between UK Universities and the British Geological Survey, <http://comet.nerc.ac.uk>) and LiCS (NE/K010867/1). Figures were plotted using the Generic Mapping Tools (GMT) (Wessel et al., 2019). We thank Yasser Maghsoudi Mehrani and Jin Fang for their invaluable assistance and constructive suggestions on our work. We thank the Editor J.P. Avouac for handling the manuscript. We also thank Hua Wang and an anonymous reviewer for their valuable comments.

Supplementary materials

Supplementary material associated with this article can be found, in the online version, at [doi:10.1016/j.epsl.2024.118919](https://doi.org/10.1016/j.epsl.2024.118919).

References

- Altamimi, Z., Rebischung, P., Métivier, L., Collilieux, X., 2016. ITRF2014: a new release of the International Terrestrial Reference Frame modeling nonlinear station motions. *J. Geophys. Res. Solid Earth* 121 (8), 6109–6131. <https://doi.org/10.1002/2016jb013098>.
- Altamimi, Z., Métivier, L., Rebischung, P., Rouby, H., Collilieux, X., 2017. ITRF2014 plate motion model. *Geophys. J. Int.* 209 (3), 1906–1912. <https://doi.org/10.1093/gji/ggx136>.
- Ansari, H., De Zan, F., Parizzi, A., 2021. Study of systematic bias in measuring surface deformation with SAR interferometry. *IEEE Transact. Geosci. Remote Sens.* 59 (2), 1285–1301. <https://doi.org/10.1109/TGRS.2020.3003421>.
- Bendick, R., Bilham, R., Freymueller, J., Larson, K., Yin, G., 2000. Geodetic evidence for a low slip rate in the Altny Tagh fault system. *Nature* 404, 69–72. <https://doi.org/10.1038/35003555>.
- Bos, M.S., Fernandes, R.M.S., Williams, S.D.P., Bastos, L., 2013. Fast Error Analysis of Continuous GNSS Observations with Missing Data. *J. Geod.* 87 (4), 351–360. <https://doi.org/10.1007/s00190-012-0605-0>.
- Bruhath, L., Fang, Z., Dunham, E.M., 2016. Rupture complexity and the supershear transition on rough faults. *J. Geophys. Res. Solid Earth* 121 (1), 210–224. <https://doi.org/10.1002/2015JB012512>.
- Cowgill, E., Yin, A., Arrowsmith, J.R., Wang, X., Zhang, S., 2004. The Akato Tagh bend along the Altny Tagh Fault, northwest Tibet; I. Smoothing by vertical-axis rotation and the effect of topographic stresses on bend-flanking faults. *Geol. Soc. Am. Bull.* 116 (11–12), 1423–1442. <https://doi.org/10.1130/B25359.1>.
- Cowgill, E., Gold, R.D., Chen, X., Wang, X., Arrowsmith, J.R., Southon, J., 2009. Low Quaternary slip rate reconciles geodetic and geologic rates along the Altny Tagh Fault, northwestern Tibet. *Geology*. 37 (7), 647–650. <https://doi.org/10.1130/G25623A.1>.
- Cowgill, E., 2007. Impact of riser reconstructions on estimation of secular variation in rates of strike-slip faulting: revisiting the Charchen River site along the Altny Tagh Fault, NW China. *Earth Planet. Sci. Lett.* 254 (3), 239–255. <https://doi.org/10.1016/j.epsl.2006.09.015>.
- Doin, M.-P., Guillaso, S., Jolivet, R., Lasserre, C., Lodge, F., Ducret, G., Grandin, R., 2011. Presentation of the small baseline NSBAS processing chain on a case example: the Etna deformation monitoring from 2003 to 2010 using Envisat data. In: *Proceedings of the Fringe 2011 Workshop*. Frascati, Italy, 19–23 September 2011.
- Du, J., Fu, B., Guo, Q., Shi, P., Xue, G., Xu, H., 2020. Segmentation and termination of the surface rupture zone produced by the 1932 Ms 7.6 Changma earthquake; new insights into the slip partitioning of the eastern Altny Tagh fault system. *Lithosphere* 12 (1), 19–39. <https://doi.org/10.1130/L1113.1>.
- Dziewonski, A.M., Chou, T.-A., Woodhouse, J.H., 1981. Determination of earthquake source parameters from waveform data for studies of global and regional seismicity. *J. Geophys. Res.* 86, 2825–2852. <https://doi.org/10.1029/JB086iB04p02825>.
- Ekström, G., Nettles, M., Dziewonski, A.M., 2012. The global CMT project 2004–2010: centroid-moment tensors for 13,017 earthquakes. *Phys. Earth Planet. Interior*. 200–201, 1–9. <https://doi.org/10.1016/j.pepi.2012.04.002>.
- Elliott, J.R., Biggs, J., Parsons, B., Wright, T.J., 2008. InSAR slip rate determination on the Altny Tagh Fault, northern Tibet, in the presence of topographically correlated atmospheric delays. *Geophys. Res. Lett.* 35 (12). <https://doi.org/10.1029/2008GL033659>.
- Elliott, A.J., Oskin, M.E., Liu-Zeng, J., Shao, Y., 2015. Rupture termination at restraining bends: the last great earthquake on the Altny Tagh Fault. *Geophys. Res. Lett.* 42 (7), 2164–2170. <https://doi.org/10.1002/2015GL063107>.
- England, P., McKenzie, D., 1982. A thin viscous sheet model for continental deformation. *Geophys. J. Int.* 70 (2), 295–321. <https://doi.org/10.1111/j.1365-246x.1982.tb04969.x>.
- Gürboğa, S., 2016. The termination of the North Anatolian fault system (NAFS) in Eastern Turkey. *Int. Geol. Rev.* 58 (12), 1557–1567. <https://doi.org/10.1080/00206814.2016.1175976>.
- Ge, W., Shen, Z., Molnar, P., Wang, M., Zhang, P., Yuan, D., 2022. GPS Determined asymmetric deformation across central Altny Tagh fault reveals rheological structure of Northern Tibet. *J. Geophys. Res. Solid Earth* 127 (9). <https://doi.org/10.1029/2022JB024216>.
- Gold, R.D., Cowgill, E., Arrowsmith, J.R., Gosse, J., Chen, X., Wang, X., 2009. Riser diachroneity, lateral erosion, and uncertainty in rates of strike-slip faulting: a case study from Tuzidun along the Altny Tagh Fault, NW China. *J. Geophys. Res. Solid Earth* 114. <https://doi.org/10.1029/2008JB005913>.
- Gold, R.D., Cowgill, E., Arrowsmith, J.R., Chen, X., Sharp, W.D., Cooper, K.M., Wang, X., 2011. Faulted terrace risers place new constraints on the late Quaternary slip rate for the central Altny Tagh Fault, northwest Tibet. *Geol. Soc. Am. Bull.* 123 (5–6), 958–978. <https://doi.org/10.1130/B30207.1>.
- Goodman, J., Weare, J., 2010. Ensemble samplers with affine invariance. *Comm. App. Math. Comp. Sci.* 5 (1), 65–80. <https://doi.org/10.2140/camcos.2010.5.65>.
- Gruber, S., 2012. Derivation and analysis of a high-resolution estimate of global permafrost zonation. *Cryosphere* 6 (1), 221–233. <https://doi.org/10.5194/tc-6-221-2012>.
- Guo, J., Wei, X., Long, G., Wang, B., Fan, H., Xu, S., 2017. Three-dimensional structural model of the Qaidam basin: implications for crustal shortening and growth of the northeast Tibet. *Open Geosci.* 9 (1), 174–185. <https://doi.org/10.1515/geo-2017-0015>.
- Harris, R.A., 2017. Large earthquakes and creeping faults. *Rev. Geophys.* 55 (1), 169–198. <https://doi.org/10.1002/2016RG000539>.
- He, J., Vernant, P., Chéry, J., Wang, W., Lu, S., Ku, W., Xia, W., Bilham, R., 2013. Nailing down the slip rate of the Altny Tagh fault. *Geophys. Res. Lett.* 40 (20), 5382–5386. <https://doi.org/10.1002/2013GL057497>.
- Herring, T.A., King, R.W., Floyd, M.A., McClusky, S.C., 2018. Technical Report. Department of Earth, Atmospheric, and Planetary Sciences, Massachusetts Institute of Technology.
- Hussain, E., Hooper, A., Wright, T.J., Walters, R.J., Bekaert, D.P.S., 2016. Interseismic strain accumulation across the central North Anatolian Fault from iteratively unwrapped InSAR measurements. *J. Geophys. Res. Solid Earth* 121 (12), 9000–9019. <https://doi.org/10.1002/2016JB013108>.
- Jolivet, R., Cattin, R., Chamot-Rooke, N., Lasserre, C., Peltzer, G., 2008. Thin-plate modeling of interseismic deformation and asymmetry across the Altny Tagh fault zone. *Geophys. Res. Lett.* 35 (2). <https://doi.org/10.1029/2007GL031511>.
- Jolivet, R., Lasserre, C., Doin, M.-P., Peltzer, G., Avouac, J.-P., Sun, J., Dailu, R., 2013. Spatio-temporal evolution of aseismic slip along the Haiyuan fault, China: implications for fault frictional properties. *Earth Planet. Sci. Lett.* 377–378, 23–33. <https://doi.org/10.1016/j.epsl.2013.07.020>.
- Kaneko, Y., Fialko, Y., Sandwell, D.T., Tong, X., Furuya, M., 2013. Interseismic deformation and creep along the central section of the North Anatolian Fault (Turkey): InSAR observations and implications for rate-and-state friction properties: modeling Interseismic strain along NAF. *J. Geophys. Res. Solid Earth*. 118, 316–331. <https://doi.org/10.1029/2012jb009661>.
- King, G., Nábělek, J., 1985. Role of fault bends in the initiation and termination of earthquake rupture. *Science* (1979) 228 (4702), 984–987. <https://doi.org/10.1126/science.228.4702.984>.
- Lazecy, M., Spaans, K., González, P.J., Maghsoudi, Y., Morishita, Y., Albino, F., Elliott, J., Greenall, N., Hutton, E., Hooper, A., Juncu, D., McDougall, A., Walters, R. J., Watson, C.S., Weiss, J.R., Wright, T.J., 2020. LICsAR: an automatic InSAR tool for measuring and monitoring tectonic and volcanic activity. *Remote Sens. (Basel)* 12 (15), 2430. <https://doi.org/10.3390/RS12152430>.
- Li, Y., Shan, X., Qu, C., Zhang, Y., Song, X., Jiang, Y., Zhang, G., Nocquet, J.-M., Gong, W., Gan, W., Wang, C., 2017. Elastic block and strain modeling of GPS data around the Haiyuan-Liupanshan fault, northeastern Tibetan Plateau. *J. Asian Earth Sci.* 150, 87–97. <https://doi.org/10.1016/j.jseas.2017.10.010>.
- Liu, C., Ji, L., Zhu, L., Zhao, C., 2018. InSAR-constrained interseismic deformation and potential seismogenic asperities on the Altny Tagh Fault at 91.5–95°E, northern Tibetan plateau. *Remote Sens. (Basel)* 10 (6). <https://doi.org/10.3390/rs10060943>.
- Li, Y., Shan, X., Qu, C., Liu, Y., Han, N., 2018. Crustal deformation of the Altny Tagh fault based on GPS. *J. Geophys. Res. Solid Earth* 123 (11), 10309–10322. <https://doi.org/10.1029/2018JB015814>.
- Li, Y., Nocquet, J.-M., Shan, X., 2022. Crustal deformation across the western Altny Tagh fault (86° E) from GPS and InSAR. *Geophys. J. Int.* 228 (2), 1361–1372. <https://doi.org/10.1093/gji/ggab403>.
- Liu, D., Li, H., Sun, Z., Pan, J., Wang, M., Wang, H., Chevalier, Marie-Luce, 2017. AFT dating constrains the Cenozoic uplift of the Qimen Tagh mountains, northeast Tibetan Plateau, comparison with LA-ICPMS Zircon U–Pb ages. *Gondwana Res.* 41, 438–450. <https://doi.org/10.1016/j.jgr.2015.10.008>.

- Liu, J., Ren, Z., Zheng, W., Min, W., Li, Z., Zheng, G., 2020. Late Quaternary slip rate of the Aksay Segment and its rapidly decreasing gradient along the Altyn Tagh Fault. *Geosphere* 16 (6), 1538–1557. <https://doi.org/10.1130/GES02250.1>.
- Luo, H., He, W., Yuan, D., Shao, Y., 2015. Slip Rate of Yema River-Daxue mountain fault since the late Pleistocene and its implications on the deformation of the northeastern margin of the Tibetan Plateau. *Acta Geol. Sinica* 89 (2), 561–574. <https://doi.org/10.1111/1755-6724.12447>.
- Mériaux, A.S., Ryerson, F.J., Tapponnier, P., Van der Woerd, J., Finkel, R.C., Xu, X., Xu, Z., Caffee, M.W., 2004. Rapid slip along the central Altyn Tagh Fault: morphochronologic evidence from Charchen He and Sulamu Tagh. *J. Geophys. Res. Solid Earth* 109 (6), B06401–B06423. <https://doi.org/10.1029/2003JB002558>.
- Mann, P., 2007. Global catalogue, classification and tectonic origins of restraining- and releasing bends on active and ancient strike-slip fault systems. *Geol. Soc. Spec. Publ.* 290 (1), 13–142. <https://doi.org/10.1144/SP290.2>.
- Morishita, Y., Lazecky, M., Wright, T.J., Weiss, J.R., Elliott, J.R., Hooper, A., 2020. LiCSBAS: an open-source insar time series analysis package integrated with the LiCSAR automated sentinel-1 InSAR processor. *Remote Sens. (Basel)* 12 (3), 424. <https://doi.org/10.3390/rs12030424>.
- Ou, Q., Daout, S., Weiss, J.R., Shen, L., Lazecký, M., Wright, T.J., Parsons, B.E., 2022. Large-scale Interseismic strain mapping of the NE Tibetan plateau from sentinel-1 interferometry. *J. Geophys. Res. Solid Earth* 127 (6). <https://doi.org/10.1029/2022JB024176>.
- Panda, D., Kundu, B., Santosh, M., 2018. Oblique convergence and strain partitioning in the outer deformation front of NE Himalaya. *Sci. Rep.* 8 (1), 10564–10569. <https://doi.org/10.1038/s41598-018-28774-3>.
- Qiao, X., Zhou, Y., 2021. Geodetic imaging of shallow creep along the Xianshuihe fault and its frictional properties. *Earth Planet. Sci. Lett.* 567, 117001. <https://doi.org/10.1016/j.epsl.2021.117001>.
- Savage, J.C., Burford, R.O., 1973. Geodetic determination of relative plate motion in central California. *J. Geophys. Res.* 78 (5), 832–845. <https://doi.org/10.1029/JB078i005p00832>.
- Shao, Y., Liu-Zeng, J., Oskin, M.E., Elliott, A.J., Wang, P., Zhang, J., Yuan, Z., Li, Z., 2018. Paleoseismic investigation of the Aksay restraining double bend, Altyn Tagh fault, and its implication for barrier-breaching ruptures. *J. Geophys. Res. Solid Earth* 123 (5), 4307–4330. <https://doi.org/10.1029/2017JB015397>.
- Shen, L., Hooper, A., Elliott, J., 2019. A spatially varying scaling method for InSAR tropospheric corrections using a high-resolution weather model. *J. Geophys. Res. Solid Earth* 124 (4), 4051–4068. <https://doi.org/10.1029/2018JB016189>.
- Stephenson, O.L., Liu, Y., Yunjun, Z., Simons, M., Rosen, P., Xu, X., 2022. The impact of plate motions on long-wavelength InSAR-derived velocity fields. *Geophys. Res. Lett.* 49 (21). <https://doi.org/10.1029/2022GL099835>.
- Styron, R., Pagani, M., 2020. The GEM Global Active Faults Database. *Earthq. Spectra* 36 (1_suppl), 160–180. <https://doi.org/10.1177/8755293020944182>.
- Wallace, K., Yin, G., Bilham, R., 2004. Inescapable slow slip on the Altyn Tagh fault. *Geophys. Res. Lett.* 31 (9), L09613–n/a. <https://doi.org/10.1029/2004GL019724>.
- Wang, H., Wright, T.J., 2012. Satellite geodetic imaging reveals internal deformation of western Tibet. *Geophys. Res. Lett.* 39 (7). <https://doi.org/10.1029/2012GL051222>.
- Wang, H., Wright, T.J., Liu-Zeng, J., Peng, L., 2019. Strain rate distribution in south-central Tibet from two decades of InSAR and GPS. *Geophys. Res. Lett.* 46 (10), 5170–5179. <https://doi.org/10.1029/2019GL081916>.
- Wang, D., Zhao, B., Li, Y., Yu, J., Chen, Y., Zhou, X., 2022. Determination of tectonic and nontectonic vertical motion rates of the North China Craton using dense GPS and GRACE data. *J. Asian Earth. Sci.* 236 (June), 105314. <https://doi.org/10.1016/j.jseas.2022.105314>.
- Watson, A.R., Elliott, J.R., Walters, R.J., 2022. Interseismic strain accumulation across the main recent fault, SW Iran, from sentinel-1 InSAR observations. *J. Geophys. Res. Solid Earth* 127 (2). <https://doi.org/10.1029/2021JB022674>.
- Weiss, J.R., Walters, R.J., Morishita, Y., Wright, T.J., Lazecky, M., Wang, H., Hussain, E., Hooper, A.J., Elliott, J.R., Rollins, C., Yu, C., González, P.J., Spaans, K., Li, Z., Parsons, B., 2020. High-resolution surface velocities and strain for Anatolia from Sentinel-1 InSAR and GNSS Data. *Geophys. Res. Lett.* 47 (17). <https://doi.org/10.1029/2020GL087376>.
- Wessel, P., Luis, J.F., Uieda, L., Scharroo, R., Wobbe, F., Smith, W.H.F., Tian, D., 2019. The Generic Mapping Tools Version 6. *Geochem. Geophys. Geosyst.* G3 20 (11), 5556–5564. <https://doi.org/10.1029/2019GC008515>.
- Withers, M., Cruden, A.R., Quigley, M.C., 2023. The development of fault networks at the termination of continental transform faults when their connecting plate boundary is “misaligned”. *Tectonics* 42 (10). <https://doi.org/10.1029/2023TC007823>.
- Wu, C., Xu, T., Tian, X., Mitchell, R.N., Lin, J., Yang, J., Wang, X., Lu, Z., 2024. Underthrusting of Tarim lower crust beneath the Tibetan plateau revealed by receiver function imaging. *Geophys. Res. Lett.* 51 (2). <https://doi.org/10.1029/2024GL108220>.
- Xiao, Q., Yu, G., Liu-Zeng, J., Oskin, M.E., Shao, G., 2017. Structure and geometry of the Aksay restraining double bend along the Altyn Tagh Fault, northern Tibet, imaged using magnetotelluric method. *Geophys. Res. Lett.* 44 (9), 4090–4097. <https://doi.org/10.1002/2017GL072581>.
- Xu, X., Tapponnier, P., Van Der Woerd, J., Ryerson, F.J., Wang, F., Zheng, R., Chen, W., Ma, W., Yu, G., Chen, G., Mériaux, A.S., 2005. Late Quaternary sinistral slip rate along the Altyn Tagh fault and its structural transformation model. *Sci. Chin. Ser. D Earth Sci.* 48, 384–397. <https://doi.org/10.1360/02yd0436>.
- Xu, X., Sandwell, D.T., Klein, E., Bock, Y., 2021. Integrated Sentinel-1 InSAR and GNSS Time-Series Along the San Andreas Fault System. *Journal of Geophysical Research: Solid Earth* 126 (11). <https://doi.org/10.1029/2021JB022579>.
- Xu, Q., Hetzel, R., Hampel, A., Wolff, R., 2021. Slip rate of the Danghe Nan Shan thrust fault from ¹⁰Be exposure dating of folded river terraces: implications for the strain distribution in Northern Tibet. *Tectonics* 40 (4). <https://doi.org/10.1029/2020TC006584>.
- Yan, B., Chen, P., Gao, Y., 2024. Stepwise decrease in strike-slip rate along the eastern Altyn Tagh Fault and its relation to the Qilian Shan thrust system, northeastern Tibetan Plateau. *J. Struct. Geol.* 179. <https://doi.org/10.1016/j.jsg.2023.105037>.
- Yang, H., Li, A., Cunningham, D., Yang, X., Zhan, Y., Chen, Z., Hu, Z., Zuo, Y., Miao, S., Sun, X., Tang, R., 2023. An evolving lithospheric-scale wrench fault system along the eastern end of the Altyn Tagh fault: kinematics and quaternary activity of the Heishan fault system, Western China. *Tectonics* 42 (3). <https://doi.org/10.1029/2023TC007764>.
- Yin, A., Dang, Y., Zhang, M., Chen, X., McRivette, M.W., 2008. Cenozoic tectonic evolution of the Qaidam Basin and its surrounding regions; (Part 3), Structural geology, sedimentation, and regional tectonic reconstruction. *Geol. Soc. Am. Bull.* 120 (7–8), 847–876. <https://doi.org/10.1130/B26232.1>.
- Youngs, R.R., Coppersmith, K.J., 1985. Implications of fault slip rates and earthquake recurrence models to probabilistic seismic hazard estimates. *Bullet. Seismol. Soc. Am.* 75 (4), 939–964. <https://doi.org/10.1785/BSSA0750040939>.
- Yu, C., Li, Z., Penna, N.T., Crippa, P., 2018. Generic atmospheric correction model for interferometric synthetic aperture radar observations. *J. Geophys. Res. Solid Earth* 123 (10), 9202–9222. <https://doi.org/10.1029/2017JB015305>.
- Yuan, Z., Liu-Zeng, J., Zhou, Y., Li, Z., Wang, H., Yao, W., Han, L., 2020. Paleoseismologic record of earthquakes along the Wuzunxiaer section of the Altyn Tagh fault and its implication for cascade rupture behavior. *Sci. Chin. Earth Sci.* 63 (1), 93–107. <https://doi.org/10.1007/s11430-019-9376-8>.
- Zhang, P.Z., Molnar, P., Xu, X., 2007. Late Quaternary and present-day rates of slip along the Altyn Tagh Fault, northern margin of the Tibetan Plateau. *Tectonics* 26 (5). <https://doi.org/10.1029/2006TC002014>.
- Zheng, G., Wang, H., Wright, T.J., Lou, Y., Zhang, R., Zhang, W., Shi, C., Huang, J., Wei, N., 2017. Crustal deformation in the India-Eurasia collision zone from 25 years of GPS Measurements. *J. Geophys. Res. Solid Earth* 122 (11), 9290–9312. <https://doi.org/10.1002/2017JB014465>.
- Zhou, J., Xu, F., Wang, T., Cao, A., Yin, C., 2006. Cenozoic deformation history of the Qaidam Basin, NW China: results from cross-section restoration and implications for Qinghai-Tibet Plateau tectonics. *Earth Planet. Sci. Lett.* 243 (1), 195–210. <https://doi.org/10.1016/j.epsl.2005.11.033>.
- Zhu, S., Xu, C., Wen, Y., Liu, Y., 2016. Interseismic deformation of the Altyn Tagh Fault determined by interferometric synthetic aperture radar (InSAR) measurements. *Remote Sens. (Basel)* 8 (3). <https://doi.org/10.3390/rs8030233>.